Iranian Journal of Astronomy and Astrophysics
Vol. 13, No. 1, Winter 2026, 15–46
©Available online at http://ijaa.du.ac.ir
DOI: 10.22128/ijaa.2026.3405.1253
Online ISSN: 2383–403X

Iranian Journal of Astronomy and Astrophysics

Research Paper

One- and Two-Dimensional Core-Collapse Supernova Simulations of a 15M$_\odot$ Progenitor using Two-Moment Neutrino Transport and the Neutrino Leakage Scheme

Khodayar Taghiniyarami*[1] · Alireza Khesali[2] · Azar Khosravi[3]

[1] Department of Theoretical Physics, Faculty of Basic Science, University of Mazandaran, P.O. Box 47416-95447, Babolsar, Iran;
*email: kiyarash.niyarami@gmail.com

[2] Department of Theoretical Physics, Faculty of Basic Science, University of Mazandaran, P.O. Box 47416-95447, Babolsar, Iran;
email: khesali@umz.ac.ir

[3] Department of Theoretical Physics, Faculty of Basic Science, University of Mazandaran, P.O. Box 47416-95447, Babolsar, Iran;
email: a.khosravi@umz.ac.ir

Received: 24 July 2026; **Accepted:** 5 October 2026; **Published:** 12 October 2026

Abstract. We investigate the evolution of a 15 $M_\odot$ core-collapse supernova (CCSN) to examine the impact of dimensionality and the efficiency of the neutrino leakage approximation. First, a 1D reference simulation is performed using `Flash-X` coupled to the `thornado` two-moment transport module. We compare this reference shock evolution with a series of 1D `FLASH 4.6.2` leakage simulations calibrated with varying neutrino-heating factors ($f_{\rm heat}$). A calibrated factor of $f_{\rm heat} = 1.60$ minimizes trajectory errors and reproduces the reference shock dynamics without triggering an artificial 1D explosion. This calibrated prescription is then applied to 2D `FLASH 4.6.2` simulations to study multidimensional shock dynamics at a reduced computational cost. In 2D, the model generates high-entropy buoyant plumes, increases the gain mass and advection timescale, and drives the ratio $\tau_{\rm adv}/\tau_{\rm heat}$ above unity. The absence of coherent growth in the lowest shock-deformation modes during the first 250 ms post-bounce indicates that shock revival is primarily driven by neutrino-driven convection rather than the standing accretion shock instability (SASI). Our results demonstrate that while the calibrated leakage scheme captures the early 1D post-bounce shock behavior, it successfully models the subsequent convection- and turbulence-driven shock expansion in 2D. This highlights that while neutrino heating provides the energy for the explosion, multidimensional convection governs how effectively this energy is retained and converted into sustained shock revival, where 1D model fails.

Keywords: Hydrodynamical Simulations , Massive Stars , Supernova Neutrinos, Hydrodynamic Instabilities, Standing Accretion Shock Instability (SASI).

1 Introduction

Core-collapse supernovae (CCSNe) represent the final evolutionary stage of massive stars with zero-age main-sequence masses greater than $\sim 8M_\odot$. These explosions, among the most

* *Corresponding author*

This is an open access article under the **CC BY** license.

energetic events in the Universe [1], produce neutron stars and black holes [2]. They are also important agents of stellar nucleosynthesis, galactic and interstellar chemical evolution [3]. With the gravitational potential energy ($\sim 2-3\times10^{53}$ erg) released at core collapse along with the production of heavy elements and compact objects, CCSNe plays a central role in much of modern theoretical astrophysics. Supernova explosions were first theorized by Baade and Zwicky, who coined the term "supernova" and hypothesized that such events arise from a normal star collapsing to form a neutron star [4]. They claimed this energy Source is released whilst neutron stars formation, explaining the high luminosities of supernovae and even argued such explosions have been critical for high-energy astrophysics and cosmic-ray origins. While the physics of stellar evolution and nuclear processes at that time were far from complete, their seminal paper laid a foundation of ideas for how core-collapse supernovae should be modeled. With the development of stellar evolution theory, it was understood that massive stars go through a series of nuclear burning phases in which lighter elements are fused increasingly into heavier ones, until an iron-group core is formed. This processes yield in iron-group nuclei with the highest binding energy per nucleon, and thus fusion reactions cannot produce further pressure to support against gravity [5]. As the iron core grows toward its effective Chandrasekhar mass, electron captures on heavy nuclei and free protons progressively decrease the electron fraction, while the photodisintegration of iron-group nuclei absorbs a significant amount of thermal energy. The combined effect of these processes substantially reduces pressure support and leading to the onset of the dynamical collapse of the stellar core [6,7].

One of the first numerical studies of CCSN was conducted by Colgate and White who pointed out that the gravitational binding energy released during the collapse exceeds the observed explosion energy by several orders of magnitude [8]. Their simulations showed that only a small fraction of this energy is needed to produce a successful explosion and proposed that neutrinos, generated in the hot and dense proto-neutron star, could efficiently transfer energy to the overlying stellar layers. This pioneering work laid the foundation for the neutrino-driven explosion mechanism which remains the prevailing theoretical framework for understanding CCSNe.

Subsequent theoretical and numerical studies demonstrated that the CCSNe explosion mechanism is far more complex than initially anticipated. Although the core bounce launches a hydrodynamic shock, the shock quickly loses much of its energy through the dissociation of infalling iron-group nuclei and persistent neutrino emission. As a result, it stalls at a radius of only a few hundred kilometers and transitions into an accretion shock instead of driving a prompt explosion. Reviving this stalled shock therefore requires an additional energy input which is now generally attributed to neutrino heating in the gain region located between the proto-neutron star (PNS) and the shock front [9–11].

Since neutrino heating and cooling govern the post-bounce evolution of the collapsing core, accurately modeling neutrino transport remains one of the central challenges in core-collapse supernova simulations. In its most rigorous form, this problem requires solving the multidimensional Boltzmann transport equation self-consistently with the hydrodynamic evolution. Such calculations, however, are computationally prohibitive because of the high dimensionality of the transport problem, especially in multidimensional simulations. This has motivated the development of a variety of approximate transport schemes that retain the essential physical processes while substantially reducing the computational expense. Among these approaches, moment-based neutrino transport methods have been developed through out recent years. A major advance was made with radiation-hydrodynamics framework in which the angular moments of the neutrino distribution are evolved using a Variable Eddington Factor closure derived from the Boltzmann equation [12,13]. Compared with direct Boltzmann solvers, this approach provides a much more computationally efficient treatment

while maintaining a high level of consistency between neutrino transport and hydrodynamics. Building on this framework, modern neutrino transport modules have evolved toward energy-dependent two-moment formulations, which are now employed in many state-of-the-art simulations of core-collapse supernovae.

Despite these advances, the computational cost of detailed neutrino transport remains a significant challenge for systematic multidimensional studies. Even on modern high-performance computing systems, simulations employing sophisticated transport algorithms demand considerable computational resources, particularly in two and three spatial dimensions. As a result, approximate transport methods continue to provide a practical alternative for investigating large sets of progenitor models and exploring how explosion properties depend on the underlying physical conditions. Among these approaches, neutrino leakage schemes [14–16] offer an effective balance between computational efficiency and physical realism. Rather than solving the full transport equations, they estimate local neutrino emission, absorption, and cooling through simplified prescriptions that capture the dominant neutrino-matter interactions. Although these methods cannot reproduce the complete angular and energy distributions of the neutrino radiation field, they have consistently been shown to recover the overall post-bounce evolution with reasonable fidelity. This combination of efficiency and robustness has made neutrino leakage schemes a widely used tool in multidimensional hydrodynamic simulations and large parameter surveys.

O'Connor & Ott [16] presented an efficient one-dimensional general-relativistic framework that incorporates a neutrino leakage scheme together with a simplified neutrino-heating prescription to follow the post-bounce evolution of massive stars. Their results showed that, despite its simplicity, the approximate transport treatment captures the overall behavior of the stalled shock while requiring only a fraction of the computational cost associated with detailed neutrino transport. They also introduced a scaling parameter for neutrino heating, providing a straightforward way to examine how variations in heating efficiency influence shock revival. This parametrized approach has since been widely adopted in studies aimed at assessing the role of neutrino energy deposition and at calibrating simplified transport models against more sophisticated neutrino-transport calculations.

Although one-dimensional simulations have provided valuable insight into the physics of core collapse, they rarely produce successful explosions for most massive progenitors when realistic microphysics is included. The primary limitation is the assumption of spherical symmetry, which suppresses the multidimensional hydrodynamic instabilities that develop naturally behind the stalled shock. Multidimensional calculations, on the other hand, capture phenomena such as neutrino-driven convection and the Standing Accretion Shock Instability (SASI), both of which increase the residence time of accreted matter within the gain region. As a consequence, neutrinos deposit energy more efficiently, creating conditions that are more favorable for shock revival. The impact of these multidimensional effects was illustrated by the high-resolution simulations of Couch and O'Connor [17], who compared one-, two-, and three-dimensional models. Their study showed that both the shock evolution and the conditions required for explosion depend strongly on the dimensionality of the simulation. In particular, turbulent motions behind the shock modify the post-shock flow and reduce the neutrino-heating threshold needed to re-energize the stalled shock. These findings underscore the importance of multidimensional simulations for understanding the neutrino-driven explosion mechanism, despite the substantial computational cost associated with realistic neutrino transport.

Due the challenges associated with multidimensional neutrino transport, this work examines the collapse of a 15 $M_\odot$ progenitor using two complementary transport approaches. We first perform one-dimensional simulations with the `Flash-X` code coupled to the `thornado` spectral two-moment neutrino transport module, which serves as the reference model for the

post-bounce shock evolution. A second set of one-dimensional simulations is then carried out with the neutrino leakage scheme implemented in `FLASH 4.6.2`, where the neutrino-heating factor is systematically varied. The resulting shock evolution is compared with the `FlashX-thornado` reference model in order to determine the heating factor that best reproduces the detailed transport solution. This calibrated heating prescription is subsequently adopted in two-dimensional `FLASH 4.6.2` simulations to investigate the multidimensional evolution of the stalled shock and the conditions leading to shock revival. In this way, the study exploits the accuracy of detailed neutrino transport for calibration while retaining the computational efficiency of the leakage scheme for multidimensional calculations.

2 Methods and The Simulation Setup

2.1 `FLASH 4.6.2` with the Neutrino Leakage Scheme

The majority of the multidimensional simulations presented in this work were performed using the `FLASH 4.6.2` [18] hydrodynamics code coupled with the multispecies neutrino leakage scheme originally implemented by O'Connor & Ott [16] and subsequently employed in multidimensional studies such as Couch [19]. The leakage approach provides an approximate treatment of neutrino transport by locally estimating neutrino emission, absorption, and diffusion processes without explicitly solving the Boltzmann transport equation. This approximation substantially reduces the computational cost while retaining the dominant neutrino cooling and heating processes responsible for the post-bounce evolution of core-collapse supernovae.

2.1.1 Hydrodynamics

The evolution of the collapsing stellar core is described by the equations of compressible hydrodynamics including self-gravity and neutrino source terms. The conservation of mass is given by

$$\frac{\partial \rho}{\partial t} + \nabla \cdot (\rho \mathbf{v}) = 0, \tag{1}$$

where ρ denotes the mass density and $\mathbf{v}$ is the fluid velocity. Momentum conservation is governed by

$$\frac{\partial (\rho \mathbf{v})}{\partial t} + \nabla \cdot (\rho \mathbf{v}\mathbf{v} + P\mathbf{I}) = -\rho \nabla \Phi, \tag{2}$$

where P is the fluid pressure and Φ represents the gravitational potential. The total energy equation can be written as

$$\frac{\partial E}{\partial t} + \nabla \cdot [(E + P)\mathbf{v}] = -\rho \mathbf{v} \cdot \nabla \Phi + Q_\nu, \tag{3}$$

where

$$E = \rho e + \frac{1}{2}\rho v^2 \tag{4}$$

is the total energy density, e denotes the specific internal energy, and Q_ν represents the net energy exchange between matter and neutrinos. Spatial reconstruction is performed using a fifth-order interpolation scheme with the hybrid slope limiter, while characteristic limiting is enabled to improve numerical stability near strong discontinuities. Artificial viscosity and shock flattening are activated to suppress spurious oscillations behind the bounce shock. The Courant-Friedrichs-Lewy number is set to CFL = 0.35 and the hydrodynamic time step

is determined automatically during the simulation. The gravitational potential is computed by solving Poisson's equation $\nabla^2\Phi = 4\pi G\rho$ which consistently couples self-gravity to the hydrodynamic evolution throughout the collapse and post-bounce phases. Self-gravity is included through the multipole Poisson solver with a maximum multipole order of $l_{\max} = 16$ providing an accurate description of the gravitational potential during collapse and the subsequent post-bounce evolution. In addition to the hydrodynamic variables, the electron fraction evolves according to

$$\frac{\partial(\rho Y_e)}{\partial t} + \nabla \cdot (\rho Y_e \mathbf{v}) = R_\nu, \tag{5}$$

where Y_e denotes the electron fraction and R_ν is the net lepton source term produced by weak interactions involving electron neutrinos and antineutrinos. Consequently, the leakage scheme affects not only the thermal evolution of the matter through Q_ν but also its composition through the evolution of Y_e. The hydrodynamic evolution is carried out on an adaptive mesh refinement (AMR) grid using a directionally unsplit finite-volume formulation [20,21]. Spatial reconstruction is performed with the fifth-order Piecewise Parabolic Method (PPM) [22], while time integration follows a second-order predictor–corrector scheme. Numerical fluxes at cell interfaces are obtained with the HLLC Riemann solver, which accurately captures shocks and contact discontinuities.

2.1.2 Deleptonization and Neutrino Leakage

Prior to core bounce, electron capture on nuclei and free protons produces a substantial flux of electron neutrinos, leading to progressive deleptonization of the collapsing core. This process reduces the electron fraction, Y_e, thereby decreasing the mass and radius of the homologously collapsing inner core [5]. Instead of solving the full neutrino transport problem during the collapse phase, we adopt the parameterized deleptonization scheme proposed by [23], in which the electron fraction is prescribed as a function of the local matter density, $Y_e(\rho)$. This approximation has been shown to reproduce the evolution of Y_e during collapse with only a weak dependence on the progenitor structure. In the present simulations, the fitting parameters corresponding to the G15 model of [23] are employed for the pre-bounce evolution.

Our leakage implementation follows exactly the O'Connor approach [24] based on the neutrino leakage prescriptions introduced by Ruffert et al. [14] and Rosswog et al. [15]. Three effective neutrino species are considered throughout the calculations: electron neutrinos (ν_e), electron antineutrinos ($\bar{\nu}_e$), and a single heavy-lepton neutrino species (ν_x). The latter represents the combined contribution of ν_μ, $\bar{\nu}_\mu$, ν_τ, and $\bar{\nu}_\tau$, since these neutrinos interact almost exclusively through neutral-current reactions during core collapse and exhibit nearly identical interaction cross sections. The transport optical depth for each neutrino species is obtained by integrating the corresponding transport opacity from the local position to the outer boundary,

$$\tau_\nu(r) = \int_r^\infty \kappa_\nu(r')\, dr', \tag{6}$$

where κ_ν denotes the total transport opacity, including both absorption and scattering contributions. Following the prescriptions of Ruffert et al. [14], the opacity is constructed from neutrino scattering on free neutrons, free protons, and heavy nuclei, together with charged-current absorption reactions of electron neutrinos and antineutrinos on nucleons.

The neutrino chemical potentials are estimated using approximate degeneracy parameters, $\eta_{\nu_i} = \mu_{\nu_i}/T$. Because heavy-lepton neutrinos remain essentially non-degenerate under

the conditions considered here, we simply adopt $\eta_{\nu_x} = 0$. For electron neutrinos, the degeneracy parameter is known in two limiting cases. Under local β-equilibrium it satisfies

$$\eta_{\nu_e}^{\rm eq} = \eta_e + \eta_p - \eta_n,$$

where the chemical potentials include the corresponding rest-mass contributions. In contrast, in the optically thin free-streaming limit the neutrino chemical potential vanishes $\eta_{\nu_e}^{\rm stream} = 0$ while the equilibrium antineutrino degeneracy parameter satisfies $\eta_{\bar{\nu}_e}^{\rm eq} = -\eta_{\nu_e}^{\rm eq}$. Since the intermediate regime cannot be described accurately without solving the full transport equations, the leakage scheme interpolates smoothly between the optically thick and optically thin limits by using the local optical depth,

$$\eta_{\nu_i} = \eta_{\nu_i}^{\rm eq} \left(1 - e^{-\tau_{\nu_i}(\eta_{\nu_i})}\right). \tag{7}$$

Because the optical depth depends on the neutrino degeneracy, while the degeneracy itself also depends on the optical depth, these quantities are evaluated iteratively until a self-consistent solution is obtained. Once the optical depths and neutrino degeneracy parameters have been determined, the leakage formalism of [15] is employed to evaluate the neutrino emission rates. The scheme includes charged-current electron and positron capture reactions,

$$p + e^- \rightarrow n + \nu_e,$$

and

$$n + e^+ \rightarrow p + \bar{\nu}_e,$$

together with thermal neutrino production through electron–positron pair annihilation and plasmon decay into neutrino–antineutrino pairs. Several modifications are introduced relative to the original implementation of Rosswog et al. [15]. First, the neutrino degeneracy parameters are taken from the optical-depth interpolation described above rather than assuming local β-equilibrium throughout the diffusion region. Second, the neutrino diffusion timescale, $t_{\rm diff}$, is multiplied by a factor of two, which provides neutrino luminosities that better reproduce reference transport calculations. Finally, instead of evaluating the thermal emission rates numerically, we adopt the analytic emissivity expressions presented by Ruffert et al. [14], which offer a computationally efficient approximation while maintaining sufficient accuracy for leakage calculations. Following the prescription of Rosswog et al. [15], the local free-emission limit and the diffusion-limited emission are combined through an interpolation formula to obtain the effective neutrino leakage rates. The effective energy-loss rate, $Q_{\rm eff}^{\rm leak}$, and the effective neutrino number-loss rate, $R_{\rm eff}^{\rm leak}$, are therefore written as

$$\chi_{{\rm eff},\nu_i}^{\rm leak} = \frac{\chi_{{\rm loc},\nu_i}^{\rm leak}}{1 + \chi_{{\rm loc},\nu_i}^{\rm leak} / \chi_{{\rm diff},\nu_i}^{\rm leak}}, \tag{8}$$

where $\chi = Q$ corresponds to the volumetric energy-loss rate ($\rm erg\,cm^{-3}\,s^{-1}$), whereas $\chi = R$ denotes the neutrino number emission rate ($\rm cm^{-3}\,s^{-1}$). This interpolation guarantees a smooth transition between optically thin regions, where neutrinos escape freely, and optically thick regions, where diffusion governs the neutrino transport and the neutrino luminosity at a given point r is given by:

$$L_{\nu_i}(r) = 4\pi \int_0^r Q_{\nu_i}^{\rm leak}(r')\, r'^2\, dr'. \tag{9}$$

To account for neutrino energy deposition behind the stalled shock, the leakage scheme is supplemented with a parameterized heating prescription that approximates charged-current

neutrino absorption in the gain region. In this layer, neutrinos begin to decouple from matter, allowing a fraction of their energy to be transferred back to the fluid and thereby contributing to shock revival. The dominant heating reactions are the absorption of electron neutrinos on free neutrons and electron antineutrinos on free protons. Following Rosswog et al. [15], the corresponding absorption cross sections are written as

$$\sigma_{\mathrm{heat},\nu_e} = \frac{(1+3g_A^2)}{4}\sigma_0 \frac{\langle \epsilon_{\nu_e}^2 \rangle_{\mathrm{ns}}}{(m_e c^2)^2} \langle 1 - f_{e^-} \rangle, \tag{10}$$

$$\sigma_{\mathrm{heat},\bar{\nu}_e} = \frac{(1+3g_A^2)}{4}\sigma_0 \frac{\langle \epsilon_{\bar{\nu}_e}^2 \rangle_{\mathrm{ns}}}{(m_e c^2)^2} \langle 1 - f_{e^+} \rangle, \tag{11}$$

where $\sigma_0 = 1.76 \times 10^{-44}\,\mathrm{cm}^2$ is the reference weak-interaction cross section, $g_A \simeq -1.25$ is the axial-vector coupling constant, and $\langle 1 - f_e \rangle$ denotes the Fermi blocking factor for the corresponding charged lepton. Under post-shock conditions the positron blocking correction is generally small, whereas electron blocking may remain important during the bounce phase. The characteristic neutrino energy entering the heating cross section is evaluated at the neutrinosphere. Following Ruffert et al.[14], the mean squared neutrino energy is taken as

$$\langle \epsilon_{\nu_i}^2 \rangle_{\mathrm{ns}} = T(\tau_{\nu_i} = 2/3)^2 \frac{F_5(\eta_{\nu_i}^{\mathrm{ns}})}{F_3(\eta_{\nu_i}^{\mathrm{ns}})},$$

where the superscript "ns" refers to quantities evaluated at the neutrinosphere, $T(\tau_{\nu_i} = 2/3)$ is the local neutrinospheric temperature, and $F_n(\eta)$ denotes the Fermi integral of order n. Using the neutrino luminosity, $L_{\nu_i}(r)$, obtained from the leakage calculation (Equation 9), the local heating rate is expressed as

$$Q_{\nu_i}^{\mathrm{heat}}(r) = f_{\mathrm{heat}} \frac{L_{\nu_i}(r)}{4\pi r^2} \sigma_{\mathrm{heat},\nu_{\mathrm{i}}} \frac{\rho}{m_u} X_i \left\langle \frac{1}{F_{\nu_i}} \right\rangle e^{-2\tau_{\nu_i}}, \tag{12}$$

where m_u is the atomic mass unit and X_i represents the mass fraction of the target particles, with X_n used for electron-neutrino absorption and X_p for electron-antineutrino absorption. The quantity $\langle 1/F_{\nu_i} \rangle$ is the inverse flux factor, which measures the anisotropy of the neutrino radiation field. Its value approaches unity in the free-streaming limit and increases as the radiation field becomes progressively more isotropic at larger optical depths. In this work, the inverse flux factor is approximated by O'Connor & Ott [24]:

$$\left\langle \frac{1}{F_{\nu_i}(\tau)} \right\rangle = 4.275\,\tau + 1.15,$$

which reproduces the expected value near the neutrinosphere while remaining consistent with detailed transport calculations in the post-shock region [25]. The exponential factor, $e^{-2\tau_{\nu_i}}$, suppresses artificial heating below the neutrinosphere where the diffusion approximation is valid, whereas the dimensionless parameter f_{heat} provides a convenient scaling of the heating efficiency. After the absorbed energy has been deposited in each computational cell, the escaping neutrino luminosity is reduced by the corresponding amount to ensure overall conservation of energy. Finally to have the right-hand side of Equations 3 and 5 we can write:

$$\begin{aligned} Q_\nu &= Q_{\mathrm{total}}^{\mathrm{heat}} - Q_{\mathrm{total}}^{\mathrm{eff,\,leak}}, \\ R_\nu &= R_{\mathrm{total}}^{\mathrm{heat}} + R_{\mathrm{total}}^{\mathrm{eff,\,leak}}. \end{aligned} \tag{13}$$

To close the hydrodynamic equations we need the equation of state (EoS) which is explained in the Section 2.3.1 and the Table 1.

2.1.3 Computational Grid

Adaptive mesh refinement (AMR) is implemented through the `PARAMESH` library [26], which dynamically adjusts the spatial resolution according to the local flow conditions. Depending on the dimensionality of the simulation, the computational domain is discretized using cylindrical coordinates in two dimensions, and spherical coordinates in one dimension. Depending on the dimensionality of the calculation, the hydrodynamic domain is represented in spherical symmetry for the 1D leakage runs and in axisymmetric cylindrical (R, Z) coordinates for the 2D calculation. Adaptive mesh refinement is provided by PARAMESH, with the highest refinement concentrated around the proto-neutron star and the post-shock region, where the strongest hydrodynamic gradients develop. The coarsest cells have a characteristic linear size of $\Delta x_{\max} = 75$ km, while the finest refinement level reaches $\Delta x_{\min} = 1.17$ km. The initial 2D hydrodynamic domain covers $R = 0$–6000 km and $Z = -6000$–6000 km. The grid used for the leakage calculation covers the central region out to 3000 km and employs 1000 radial zones and 37 angular zones. The radial refinement is progressively relaxed toward larger radii, providing high spatial resolution in the PNS and gain regions without requiring a uniformly fine mesh throughout the computational domain (Figure 1). Figure 1 compares the computational grids used in the simulation. Panel (a) shows the initial `FLASH` AMR mesh in the R–Z plane, covering $R = 0$–6000 km and $Z = -6000$–6000 km, while panel (b) shows the mesh adopted for the leakage scheme calculation over the smaller domain $R = 0$–3000 km and $Z = -3000$–3000 km. In both cases, the grid is strongly refined near the origin where the PNS and the steepest hydrodynamic gradients are located. The resolution decreases progressively with radius producing a quasi-radial refinement pattern that concentrates computational effort in the central regions. This layout allows the collapse, bounce, and early post-bounce dynamics to be resolved efficiently without using a uniformly fine mesh throughout the entire stellar envelope. The larger AMR domain ensures that the infalling outer layers remain within the computational volume whereas the leakage grid focuses on the region most relevant for neutrino cooling and heating. Together these meshes provide an efficient compromise between accuracy in the core and cost control at large radii.

2.2 `Flash-X` with Spectral Two-Moment Neutrino Transport in `thornado`

To establish a reliable reference model for the evolution of the supernova shock, we perform one-dimensional core-collapse simulations with the `Flash-X` [1] [27] framework coupled to the `thornado` [28] neutrino transport library. In this approach the hydrodynamic evolution of the stellar core is solved simultaneously with the transport of neutrino radiation, allowing for a self-consistent treatment of the exchange of energy, momentum, and lepton number between matter and neutrinos. Such a coupled radiation–hydrodynamic description is essential for accurately modeling the collapse of the iron core, the formation of the proto-neutron star, and the subsequent evolution of the stalled shock. Since neutrino heating is responsible for depositing energy behind the shock, the accuracy of the transport scheme plays a decisive role in determining the onset of shock revival.

In this study we carry out one-dimensional simulations of CCSN in which the evolution of the stellar fluid is solved simultaneously with neutrino radiation transport and self-gravity. The calculations follow the entire sequence from the onset of iron-core collapse through core bounce, the formation of the PNS, and the subsequent evolution of the stalled shock. Since neutrinos dominate the transport of energy and lepton number during these phases, their

[1] `https://flash-x.org/`

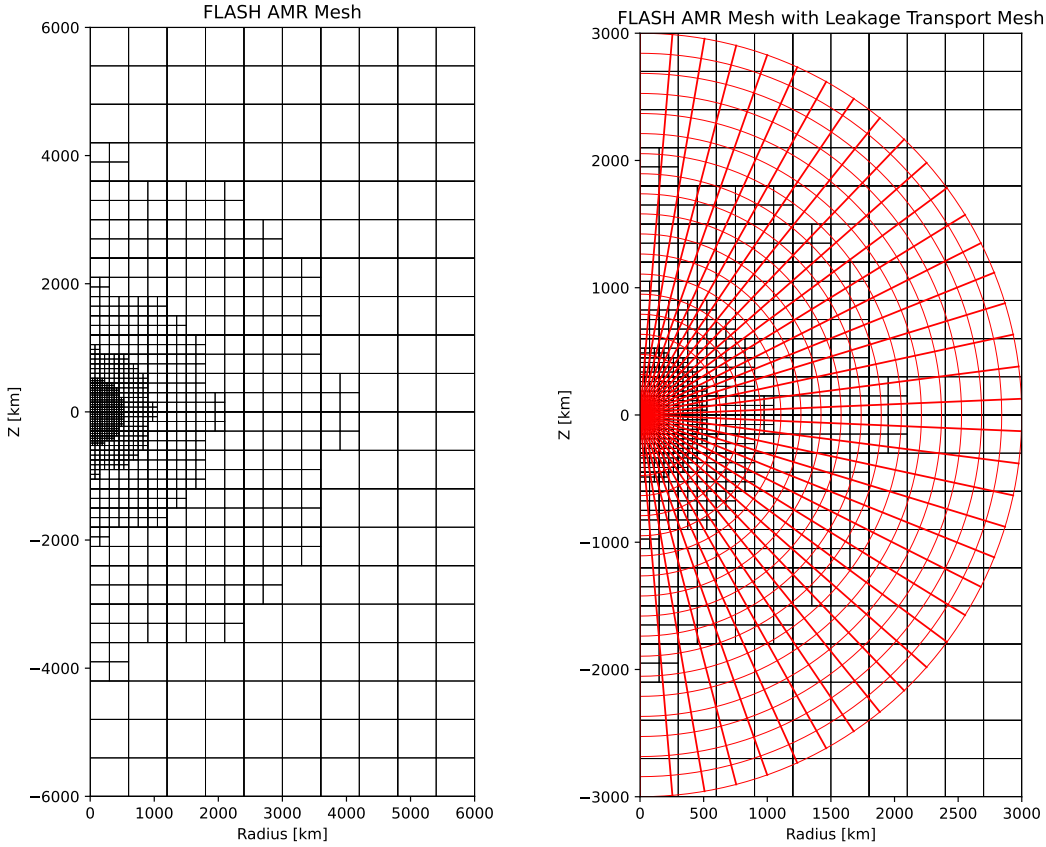

Figure 1: Comparison of the computational meshes used in the simulation. Panel (a) shows the initial FLASH adaptive mesh refinement grid at the onset of collapse in the R–Z plane, spanning $R = 0$–6000 km and $Z = -6000$–6000 km. Panel (b) shows the mesh used for the leakage-transport calculation over the smaller domain $R = 0$–3000 km and $Z = -3000$–3000 km. In both cases, the mesh is concentrated near the origin and becomes progressively coarser at larger radii.

interaction with matter largely determines the thermal state of the post-shock region and the possibility of shock revival.

2.3 Radiation hydrodynamics

Our simulations are performed within the multiphysics `Flash-X` framework, which couples hydrodynamics, self-gravity, the equation of state, and neutrino transport in a fully integrated computational environment. The fluid is evolved using the Newtonian Euler equations in conservative form,

$$\frac{\partial \rho}{\partial t} + \partial_i(\rho v^i) = 0, \tag{14}$$

$$\frac{\partial(\rho Y_e)}{\partial t} + \partial_i(\rho Y_e v^i) = -m_B Q_L, \tag{15}$$

$$\frac{\partial(\rho v_i)}{\partial t} + \partial_j(\rho v_i v^j + p\delta_i^{\,j}) = -\rho\partial_i\phi - Q_{M_i}, \tag{16}$$

$$\frac{\partial e_t}{\partial t} + \partial_i\left[(e_t + p)v^i\right] = -\rho v^i\partial_i\phi - Q_E. \tag{17}$$

Here, ρ is the mass density, v^i the velocity field, Y_e the electron fraction, p the gas pressure, and e_t the total energy density. The source terms Q_L, Q_{M_i}, and Q_E represent neutrino-mediated exchange of lepton number, momentum, and energy, respectively. we can re-write these equations as follows [29]:

$$\partial_t\boldsymbol{\mathcal{U}} = T(\boldsymbol{\mathcal{U}}, \Phi) \tag{18}$$

where $\boldsymbol{\mathcal{U}}$ is the cell averaged solution vector containing information about both fluid and radiation. The right-hand side $T(\boldsymbol{\mathcal{U}}, \Phi)$ refers to the finite-volume (FV) [30] representation of space derivatives known as convection terms including the gravity potential Φ. Self-gravity is computed by solving Poisson's equation with a multipole expansion of the gravitational potential. In our implementation, the multipole order is truncated at $\ell_{\max} = 16$.

Since we can write $\boldsymbol{\mathcal{U}}$ in the form of $\boldsymbol{\mathcal{U}} = (\boldsymbol{u}, \boldsymbol{M})$ where $\boldsymbol{u}$ and $\boldsymbol{M}$ represents fluid and radiation filed respectively. For the radiation field one can solve the Boltzmann equation in the form of radiation moments [31]:

$$\partial_t(\mathcal{D} + v^i\mathcal{I}_i) + \partial_i(\mathcal{I}^i + v^i\mathcal{D}) - \frac{1}{\epsilon^2}\frac{\partial}{\partial\epsilon}\left(\epsilon^3\mathcal{K}^i_j\nabla_i v^j\right) = \frac{1}{4\pi}\int\mathcal{C}(f)\frac{\mathrm{d}\mathbf{p}}{\epsilon}. \tag{19}$$

$$\partial_t(\mathcal{I}_j + v^i\mathcal{K}_{ij}) + \partial_i(\mathcal{K}^i_j + v^i\mathcal{I}_j) - \frac{1}{\epsilon^2}\frac{\partial}{\partial\epsilon}\left(\epsilon^3\mathcal{Q}^i_{kj}\nabla_i v^k\right) - \mathcal{Q}^i_{kj}\nabla_i v^k + \mathcal{I}^i\nabla_i v_j = \frac{1}{4\pi}\int\mathcal{C}(f)\hat{p}_j\frac{\mathrm{d}\mathbf{p}}{\epsilon}, \tag{20}$$

where the moments are defined as:

$$\left\{\mathcal{D}, \mathcal{I}^\mu, \mathcal{K}^{\mu\nu}, \mathcal{Q}^{\mu\nu\rho}\right\}_{(\epsilon,\boldsymbol{x},t)} = \frac{1}{4\pi}\int f(\boldsymbol{p}, \boldsymbol{x}, \epsilon, t)\left\{1, \hat{p}^\mu, \hat{p}^\mu\hat{p}^\nu, \hat{p}^\mu\hat{p}^\nu\hat{p}^\rho\right\}\mathrm{d}\Omega_{\hat{p}}, \tag{21}$$

which f is the distribution function which preserves the realizability of fermion statistic of $0 \leq f \leq 1$ (see [32] for more details), v^i denotes the fluid velocity measured in the laboratory frame and ϵ is the neutrino energy in the comoving frame. The energy-derivative terms appearing in these equations account for energy-space advection arising from Doppler shifts and compression or expansion of the moving fluid. $\boldsymbol{p}$ and $\boldsymbol{x}$ denote the momentum and spatial coordinates, respectively, t represent time and $\hat{p}$ is the direction of the neutrino beam and $\mathcal{C}$ is the collision term. One can re-write Equations 19 and 20 as follows [29]:

$$\partial_t\boldsymbol{M} = T_M(\boldsymbol{M}) + C_M(\boldsymbol{M}, \boldsymbol{u}). \tag{22}$$

where $T_M(\boldsymbol{M})$ is the transport operator (space derivatives) and $C_M(\boldsymbol{M}, \boldsymbol{u})$ is the collision operator which couples the radiation and fluid via [29]:

$$\partial_t\boldsymbol{u} = \boldsymbol{C}_u(\boldsymbol{M}, \boldsymbol{u}), \tag{23}$$

where $\boldsymbol{C}_u(\boldsymbol{M}, \boldsymbol{u})$ has the right-hand side of the Equations 16 and 17 The source terms Q_L, Q_{M_i}, and Q_E. The moment Equations 19 and 20 are evolved with Discontinuous Galerkin (DG) method (see [32–34]) by `thornado` with the Minerbo analytic closure to close the moment equations.

In the high-density regions of the computational domain, neutrino–matter interactions occur on very short timescales and make the source terms stiff. To handle this stiffness efficiently, we adopt an implicit–explicit (IMEX) time-integration strategy [33]. In this approach, the coupling terms are treated implicitly, which allows stable evolution even when

the timestep is much larger than the characteristic interaction timescale, whereas the transport and advection operators, T_u and T_M, are advanced explicitly. A first-order IMEX update from t^n to $t^{n+1} = t^n + \Delta t$ for Equations 18, 22, adn 23 is written as [29]:

$$\boldsymbol{\mathcal{U}}^* = \boldsymbol{\mathcal{U}}^n + \Delta t\, T_u(\boldsymbol{\mathcal{U}}^n, \Phi^n), \tag{24}$$

$$\boldsymbol{M}^* = \boldsymbol{M}^n + \Delta t\, T_M(\boldsymbol{M}^n), \tag{25}$$

$$\boldsymbol{u}^{n+1} = \boldsymbol{u}^* + \Delta t\, C_u(\boldsymbol{M}^{n+1}, \boldsymbol{u}^{n+1}), \tag{26}$$

$$\boldsymbol{M}^{n+1} = \boldsymbol{M}^* + \Delta t\, C_M(\boldsymbol{M}^{n+1}, \boldsymbol{u}^{n+1}). \tag{27}$$

Higher-order time accuracy can be obtained by extending this formulation to multi-stage diagonally implicit Runge–Kutta IMEX schemes [35], although we do not present those details here. Because the radiation-transport timestep is smaller than, and not tied to, the global timestep of the main `Flash-X` evolution loop, the transport update is subcycled in time. During this procedure, the radiation solver is advanced repeatedly until the target global timestep is reached, with boundary-cell data refreshed between successive substeps.

The hydrodynamic update is carried out with the directionally unsplit SPARK finite-volume Godunov solver [36]. Spatial reconstruction is performed using fifth-order WENO [37], and time integration is based on strong-stability-preserving Runge–Kutta methods. Unless otherwise stated, we adopt a Courant factor of 0.4. To improve robustness, a hybrid limiter is employed. The monotonized-central limiter is used for nearly linear characteristic fields, while the minmod limiter is applied to more nonlinear wave families. The calculations are carried out in spherical symmetry with adaptive mesh refinement provided by PARAMESH 4.1 [38]. Reflective boundary conditions are imposed at the inner boundary, while outflow conditions are used at the outer boundary.

2.3.1 Equation of State and Weak Interactions

The thermodynamic evolution of the collapsing stellar core is governed by the adopted equation of state (EoS) together with the weak interaction processes that regulate neutrino production, absorption, and scattering. These microphysical ingredients determine the thermodynamic response of dense matter and control the exchange of energy, momentum, and lepton number between the fluid and the neutrino radiation field throughout the collapse and the early post-bounce evolution.

In the present work, the nuclear equation of state is taken from the SFHo model [39], which is provided through the tabulated data distributed with `WeakLib` [2]. The SFHo EoS has been constructed to reproduce both nuclear experimental constraints and astrophysical observations, including measurements of photospheric radius-expansion (PRE) X-ray bursts and low-mass X-ray binaries (LMXBs). In particular, the underlying nuclear parameters, such as the incompressibility and the symmetry energy, are consistent with current theoretical and experimental estimates. The thermodynamic coverage of the adopted EoS together with the tabulation resolution in each dimension is summarized in Table 1.

An important consideration in selecting an equation of state for core-collapse supernova simulations is its consistency with the observed properties of neutron stars. For a cold, spherically symmetric neutron star in hydrostatic equilibrium, the stellar structure is determined by the Tolman–Oppenheimer–Volkoff (TOV) equations. For an equation of state that provides the pressure as a function of the mass-energy density, the TOV equations can be written as

[2] `https://github.com/starkiller-astro/weaklib`

$$\frac{dP}{dr} = -\frac{G}{r^2}\left(\rho + \frac{P}{c^2}\right)\left(m + \frac{4\pi r^3 P}{c^2}\right)\left(1 - \frac{2Gm}{rc^2}\right)^{-1} \tag{28}$$

together with the enclosed-mass equation

$$\frac{dm}{dr} = 4\pi r^2 \rho. \tag{29}$$

Here, $m(r)$ denotes the gravitational mass enclosed within radius r, P is the pressure, ρ is the mass-energy density, G is the gravitational constant, and c is the speed of light. For a specified equation of state and a chosen central density, integration of Equations (28) and (29) from the stellar center to the surface, defined by $P(R) = 0$, determines the stellar mass $M = m(R)$ and radius R. Repeating this procedure for different central densities produces the corresponding neutron-star mass–radius relation, $M(R)$. Thus, an EoS does not prescribe the mass–radius relation directly; rather, its pressure–density relation determines the M–R sequence through the relativistic stellar-structure equations.

The SFHo model was specifically constructed to provide a description of dense nuclear matter that is compatible with both nuclear-physics constraints and astrophysical observations [40]. Its relatively compact neutron-star configurations distinguish it from several traditionally used supernova equations of state. For cold beta-equilibrated matter, SFHo predicts a radius of approximately 11.9 km for a $1.4\,M_\odot$ neutron star and a maximum gravitational mass of approximately $2.06\,M_\odot$ [40]. The corresponding mass–radius sequence is consistent with the observational constraints used in constructing the model. Figure 2 illustrates the mass–radius relation predicted by SFHo together with representative constraints inferred from neutron-star observations [39,40].

The relevance of the EoS to the present core-collapse calculations extends beyond the cold neutron-star mass–radius relation. During collapse and the post-bounce evolution, matter spans a broad range of densities, temperatures, and compositions and is generally far from cold beta equilibrium. The EoS therefore enters the simulations in tabulated finite-temperature form, providing the required thermodynamic quantities as functions of (ρ, T, Y_e),

$$P = P(\rho, T, Y_e), \qquad \epsilon = \epsilon(\rho, T, Y_e), \qquad s = s(\rho, T, Y_e), \tag{30}$$

where P, ϵ, and s denote the pressure, specific internal energy, and specific entropy, respectively. The stiffness of the EoS influences the compactness and contraction of the proto-neutron star and consequently affects the post-bounce hydrodynamics, neutrino emission, and shock evolution. The thermodynamic ranges and tabulation resolutions adopted for SFHo in the present simulations are summarized in Table 1. The neutrino interaction rates included in this study comprise four classes of weak processes: (i) charged-current absorption and emission on free nucleons and heavy nuclei, (ii) coherent isoenergetic scattering on nucleons and nuclei, (iii) non-isoenergetic scattering with electrons, and (iv) neutrino pair production and annihilation. A summary of the interaction channels employed in the transport calculation is presented in Table 2. For the non-isoenergetic scattering and pair processes, both incoming and outgoing neutrino energy states are treated consistently. All interaction rates are based on the formalism developed by [41] and are tabulated within `WeakLib`, where interpolation is used to evaluate the corresponding neutrino mean free paths during the simulation.

All neutrino opacities are tabulated within the `WeakLib` library, where they are defined on the same thermodynamic grid as the SFHo equation of state, ensuring a consistent interpolation of both thermodynamic quantities and interaction rates throughout the simulation.

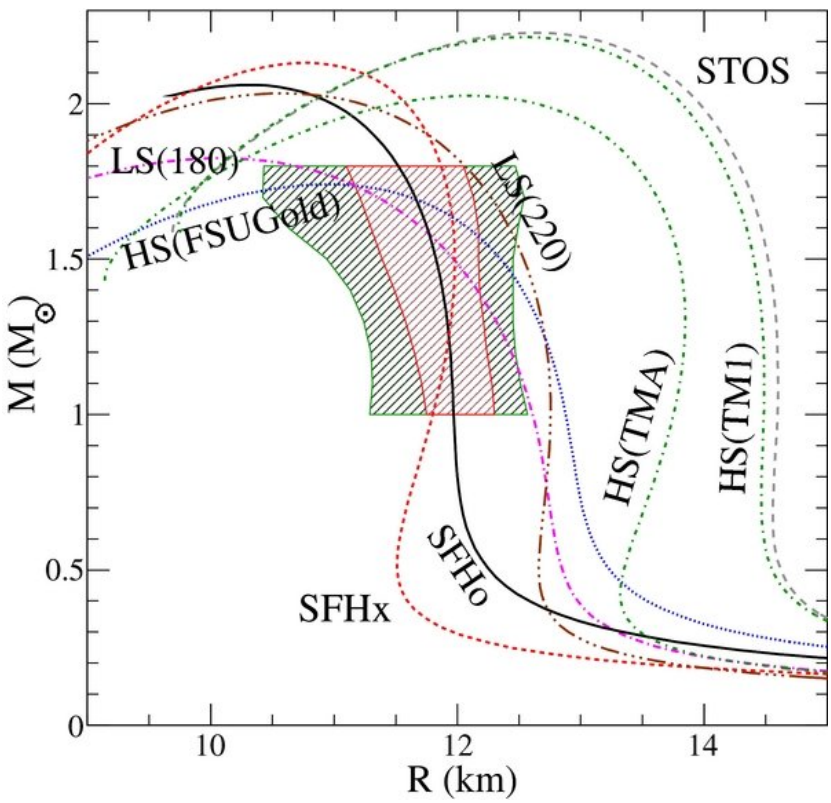

Figure 2: Neutron-star mass–radius relations for SFHo and representative equations of state used in core-collapse supernova calculations. The shaded regions indicate observationally inferred constraints on neutron-star masses and radii. The SFHo sequence lies within the observationally favored region over the typical neutron-star mass range. Figure adapted from [40]. see also [39].

Table 1: Thermodynamic ranges and tabulation resolution adopted for the SFHo equation of state.

Thermodynamic Variable	**Range**	**Resolution (Points per Decade)**
Density, ρ	$1.66 \times 10^4 - 3.16 \times 10^{15}$ g cm^{-3}	15
Temperature, T	$1.16 \times 10^9 - 1.84 \times 10^{12}$ K	25
Electron Fraction, Y_e	0.01 – 0.60	50

In the present calculations, the transport is restricted to electron neutrinos (ν_e) and electron antineutrinos ($\bar{\nu}_e$), since these species dominate the exchange of lepton number and energy during the collapse, core bounce, and the early post-bounce evolution. They participate directly in the charged-current weak interactions responsible for deleptonization and for the evolution of the electron fraction, Y_e. Heavy-lepton neutrinos (ν_μ, $\bar{\nu}_\mu$, ν_τ, and $\bar{\nu}_\tau$), whose interactions are mediated primarily through neutral-current processes, are expected to have a comparatively smaller influence under the thermodynamic conditions considered in this study. Although thermal production of heavy-lepton neutrinos becomes increas-

Table 2: Weak interaction processes included in the neutrino transport calculations.

Type	**Weak Interaction**
Absorption / Emission	$\nu_e + n \rightleftharpoons e^- + p$
	$\bar{\nu}_e + p \rightleftharpoons e^+ + n$
	$\nu_e + A \rightleftharpoons e^- + A'$
Coherent Scattering	$\nu + A \rightarrow \nu + A$
	$\nu + N \rightarrow \nu + N$
Non-isoenergetic Scattering	$\nu + e^- \rightleftharpoons \nu + e^-$
Pair Creation / Annihilation	$e^- + e^+ \rightleftharpoons \nu + \bar{\nu}$

ν_e and $\bar{\nu}_e$ denote the electron neutrino and antineutrino, respectively. Here, ν refers to either ν_e or $\bar{\nu}_e$, n and p are free neutrons and protons, N is a free nucleon, and A and A' denote nuclei.

ingly important at sufficiently high temperatures and neutrino energies, explicitly evolving these species is not required for the 9–25 $M_\odot$ progenitor models investigated here. In this work we consider a set of non rotating solar metallicity presupernova models with zero-age main-sequence mass $15M_\odot$ adopted from [42].

2.3.2 Grid and Domain

The one-dimensional Flash-X/thornado calculation is performed in spherical symmetry. The progenitor center is located at the origin ($r = 0$), where a reflective boundary condition is imposed, while an outflow boundary condition is applied at the outer radial boundary ($r = r_{\max}$), allowing matter and radiation to leave the computational domain.

The spatial discretization employs the block-structured Adaptive Mesh Refinement (AMR) infrastructure provided by PARAMESH. The radial mesh is initialized with 15 blocks and 16 zones per block (`nblockx` = 15 and `nxb` = 16), with refinement levels ranging from $l_{\min} = 1$ to $l_{\max} = 6$. Refinement is concentrated toward the central region and around strong hydrodynamic gradients in order to resolve the proto-neutron star, shock front, and post-shock structure efficiently.

The treatment of neutrino energy differs fundamentally between the two transport approaches employed in this work. In the leakage calculations, neutrino radiation is not evolved on an explicit spectral energy grid. Instead, the emission, diffusion, and absorption rates are evaluated from local thermodynamic quantities together with energy-integrated neutrino quantities and characteristic neutrino energies, as described in Section 2.1.2. Thus, no discrete neutrino energy groups are evolved in the leakage scheme. In contrast, the thornado two-moment calculation treats the neutrino radiation spectrally. The neutrino-energy domain is discretized using the same discontinuous Galerkin (DG) framework employed for the radiation moments. We use 16 geometrically spaced physical DG energy elements spanning 0.1–300 MeV. A linear representation is adopted within each energy element, corresponding to two DG nodal values per element. We therefore refer to the 16 physical DG elements as 16 neutrino energy groups, rather than counting the individual DG nodes as separate energy groups. The element widths increase geometrically toward higher neutrino energies, with the first and last physical elements having widths of approximately 2.172 MeV and 61.74 MeV,

respectively. This spectral discretization allows the two-moment calculation to follow the energy dependence of neutrino transport and neutrino–matter interactions explicitly.

3 Results

3.1 The evolution of the 15 $M_\odot$ with the two-moment model

Figure 3 shows the time evolution of density, electron fraction, radial velocity, and specific entropy versus the stellar radius during the collapse and early post-bounce evolution of the 15 $M_\odot$ progenitor simulated with `Flash-X` coupled to `thornado`. The curves are color-coded by time relative to core bounce, spanning approximately −170 to +240 ms. In the upper

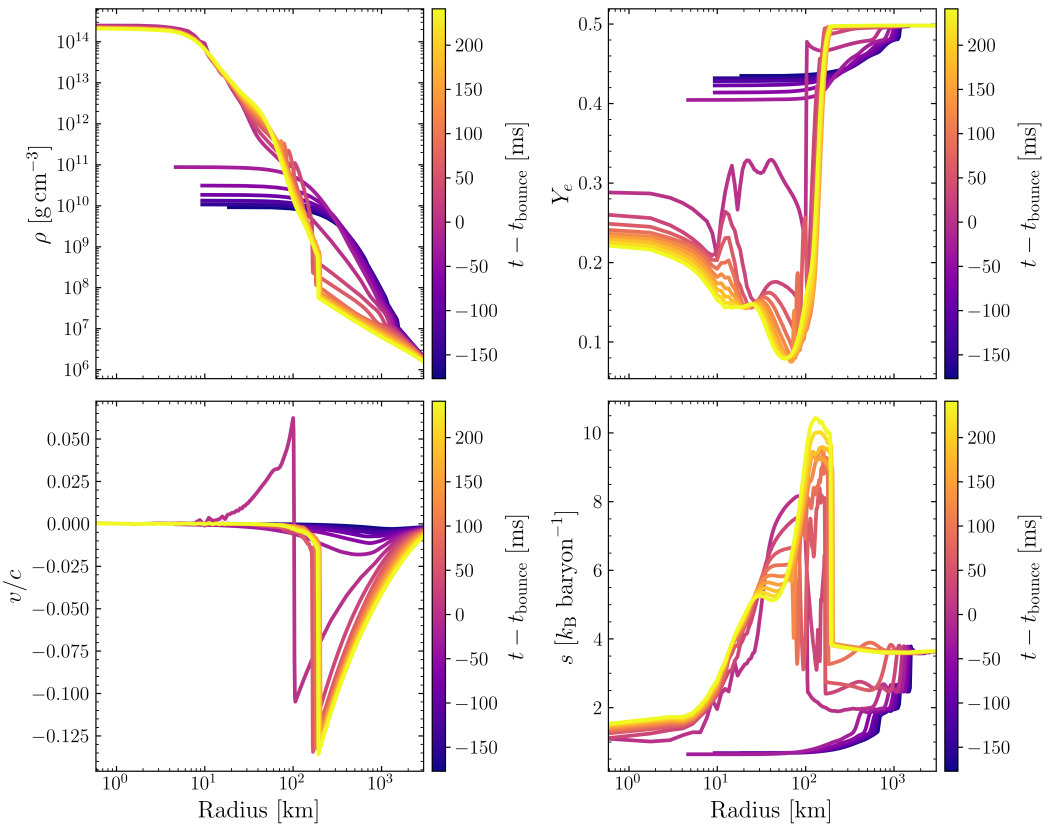

Figure 3: The time evolution of 15$M_\odot$ progenitor radial profiles of density (upper-left), electron fraction(upper-right), velocity profile (lower-left), and the entropy (lower-right) of the Figure. Dark blue color in the color-bar shows onset of the collapse and the purple color shows starts of the core-bounce and yellow color indicates the profiles at the more than 200 ms post-bounce.

left of the Figure 3, the density of the inner stellar core (≈ 10 to 100 km) at the onset of collapse is of the order of $\mathcal{O}(10^{10})$ g cm^{-3} and as the collapse starts it reaches to the point of nuclear density of the order $\mathcal{O}(10^{14})$ g cm^{-3}. From this moment , where PNS is formed, until 200 ms post-bounce the density of the inner core does not change drastically

and the stellar core remains at the central density of $\rho_c \sim 2 \times 10^{14}$ g cm^{-3}. The core bounce happens at the density of 3×10^{14} g cm^{-3}. At bounce as the inner core stiffens and nuclear saturation density is approached, the core halts the collapse and launching a hydrodynamic shock. This transition is visible in the velocity profiles (lower-left in the Figure 3) as a sharp change from negative infall velocity ($\sim -0.1c$) to a positive outward velocity ($\sim 0.07c$) near radii of order 100 km. At the later times one can see that the positive velocity becomes negative ($\sim -0.125c$) and discontinuity is still there and it shows accretion shock and prevent stellar core to explode. As the shock passage (right after the bounce) through the outer layers (10 to 100 km), it also produces a pronounced entropy jump (visible in the lower-right of Figure 3). Post-shock matter is heated and compressed, and the entropy rises to values of several k_B per baryon, with local maxima exceeding $s \sim 8$–$10\, k_B$ baryon^{-1} in the shocked region. In the post-bounce phase the shock propagates outward but does not immediately lead to an explosion. Instead, it encounters the accreting outer mass shells and progressively loses energy, leading to a stalled shock configuration at radii of order 150 to 200 km in the first 50 ms after bounce (Figure 5). This is evident from the persistence of a sharp transition in both velocity and entropy near those radii across the late time profiles. Behind the shock, matter remains hot and partially processed by neutrino interactions which drives the entropy upward relative to the infalling pre-shock material. The radial velocity structure shows a coexistence of outward-moving or slowly expanding post-shock gas and continuing infall in the outer layers, which is the expected accretion shock configuration in the early post-bounce phase.

The Y_e evolution (upper-right of Figure 3) after bounce is showing the delepotonization due neutrino emissions. Matter passing through the shock and the nascent proto-neutron-star environment is subject to intense neutrino emission and absorption, which modifies the local electron fraction. A deep trough is visible behind the shock due to the neutrino-burst (0-50 ms). In the post-shock region ($\sim$ 100 km) the profiles show a tendency toward higher Y_e compared with the deleptonized inner core ($\sim$ 10 to 100 km), reflecting the interplay between neutrino-matter interactions, shock reheating, and the thermodynamic readjustment of the accreted material. Overall, Figure 3 demonstrates that the `FLASH-X+thornado` calculation reproduces the standard qualitative features of core collapse with physically consistent evolution of the hydrodynamic and compositional variables. The density steepening, deleptonization, bounce-driven shock launch, entropy production, and stalled-shock accretion phase are all clearly resolved.

Figure 4 summarizes the post-bounce evolution of the mass-accretion rate and luminosity at four representative radii, $R = 200$, 250, 300, and 350 km. The accretion rate profiles decline systematically with post-bounce time as shock forms and starts to propagate outwards, decreasing from values of order 1–10 $M_\odot\,\mathrm{s}^{-1}$ at early times to a few $10^{-1}\, M_\odot\,\mathrm{s}^{-1}$ by $\sim$ 250 ms. The curves at 250–350 km are comparatively smooth and converge after the first $\sim$ 40–60 ms, indicating that the outer post-shock accretion flow becomes progressively more uniform as the system evolves. In contrast, the 200-km profile shows pronounced short time variability in the first few tens of milliseconds and two distinct excesses around $\sim$ 100–125 ms and $\sim$ 135–160 ms, reflecting transient structure in the inner post-shock region and the non-steady nature of the accretion flow close to the proto-neutron star. The luminosity panel in the first 50 ms post-bounce shows an abrupt increase of neutrino luminosity which corresponds to the shock pass through the outer layer that causes the drop of the opacity and consequently free neutrino stream out of the core. After that the shock stalls again and causes also prevent much more accretion onto the proto-neutron star which shows gradual decrease of the neutrino luminosity.

The entropy map in Figure 5 provides a complementary view of the same post-bounce dynamics by tracking the redistribution of thermodynamic structure in the time–radius

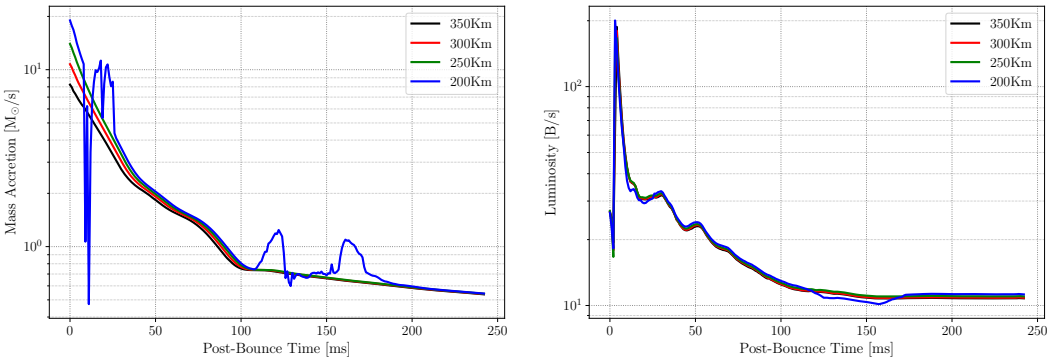

Figure 4: Post-bounce evolution of the mass-accretion rate and luminosity at $R = 200$, 250, 300, and 350 km. The left panel shows the mass-accretion rate as a function of post-bounce time over 0–250 ms on a logarithmic scale. The outer-radius profiles are comparatively smooth and converge at late times, while the 200-km profile exhibits early-time variability (due to the bounce and the shock passage) and two transient enhancements (competition between shock and accretion) at intermediate times. The right panel shows the corresponding luminosity evolution at the same radii over the same time interval. The logarithmic ordinate is labeled as in the supplied figure.

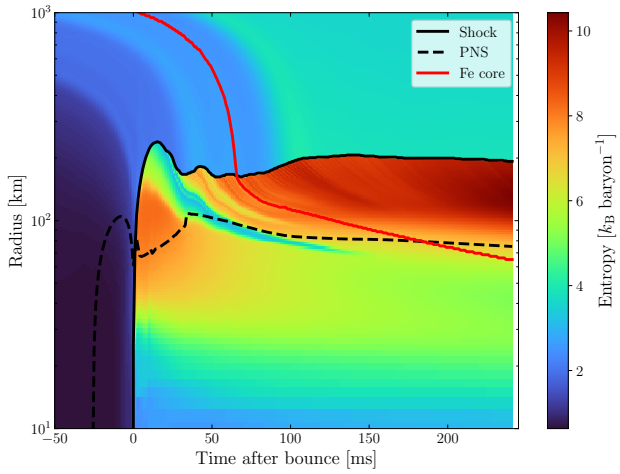

Figure 5: Time–radius evolution of the specific entropy for the 15 $M_\odot$ progenitor model during collapse and the early and the late post-bounce phase. The color map shows the entropy in units of k_B baryon^{-1}, with low-entropy infalling iron-core material (prior to the bounce) at large radii and a high entropy region forming behind the shock after bounce. The solid black curve marks the shock radius, the dashed black curve shows the PNS radius, and the red curve traces the iron-core interface.

plane. The color scale shows that low-entropy material from the infalling iron core (in the dark blue color) prior to bounce, while the onset of core bounce drives the inner region toward higher entropy through compression and shock heating. Immediately after bounce, a clearly identifiable high-entropy layer forms behind the shock, marking the shocked post-bounce region where dissipation and neutrino-matter interactions raise the thermodynamic

entropy. The shock trajectory, overplotted as a solid black curve shows the outer boundary of this heated region and highlights the transition from the infalling to the post-shock flow. The dashed black curve corresponding to the proto-neutron-star radius remains well inside the shock at all times, illustrating the compactness of the central remnant during the early post-bounce phase. In contrast, the red curve traces the collapsing iron-core interface, which moves rapidly inward as the pre-shock material continues to accrete and the shock traverses the iron core at 70 ms. The separation between these three curves emphasizes the layered structure of the system at the post-bounce time. The newly formed PNS, the shock-heated gain and post-shock layers, and the pre-shock accretion materials. As time progresses, the high-entropy region behind the shock becomes more spatially extended, reflecting ongoing accretion, shock reprocessing, and neutrino-driven heating. These features show that the entropy distribution is a sensitive diagnostic of shock revival conditions and of the evolving coupling between accretion and neutrino emission in the post-bounce phase.

3.2 Shock Radius Evolution Comparison of the Two-Moment and the Leakage Scheme

Figure 6 shows the post-bounce evolution of the shock radius over the first 300 ms after core bounce for a black solid line references to Two-Moment model and the rest are according to the leakage scheme calculations with different heating factors, f_{heat}. The black curve labeled as Two-Moment exhibits the familiar early expansion of the shock to a radius of approximately 200–250 km within the first $\sim$ 20–30 ms, followed by a recession phase and then a comparatively stable evolution around $\sim$ 190–200 km at later times. This behavior is consistent with a stalled shock configuration that remains extended relative to the more weakly heated leakage runs (with the heating factors lower than 1.7).

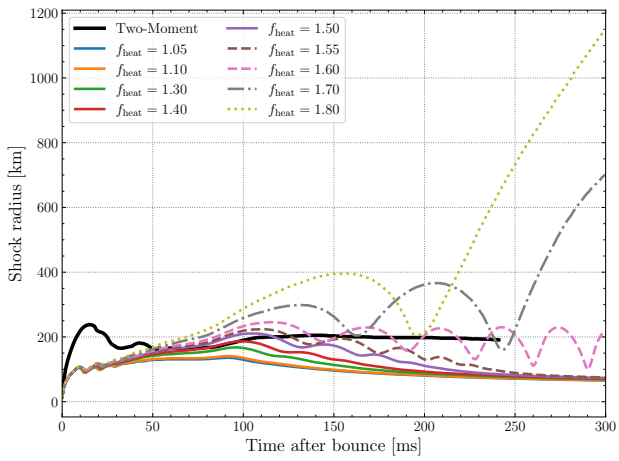

Figure 6: Evolution of the shock radius as a function of post-bounce time for the reference Two-Moment model and the leakage calculations with different heating factors, f_{heat}. The Two-Moment solution reaches an early maximum shock radius of about 200–250 km and later remains near $\sim$ 200 km, while the leakage models with $f_{\mathrm{heat}} = 1.05$–1.50 expand initially but subsequently recede to smaller radii. As the heating factor increases the leakage runs develop progressively larger shock excursions and stronger oscillations. The $f_{\mathrm{heat}} = 1.70$ and 1.80 models show late-time shock revival, with the $f_{\mathrm{heat}} = 1.80$ case reaching $\sim$ 1200 km by 300 ms.

The leakage models with $f_{\rm heat} = 1.05$–1.50 show a broadly similar qualitative sequence during the early post-bounce phase. An initial expansion, a peak shock radius in the range of roughly 140–210 km, and a subsequent contraction. However, unlike the Two-Moment curve, these models generally continue to recede and approach smaller shock radii, reaching values of order $\sim$ 70–100 km by the end of the plotted interval. In this sense the main difference relative to the two-moment reference is not the existence of the initial shock expansion itself, but the ability of the model to sustain a larger average shock radius at late times. The two-moment evolution remains systematically more extended whereas the low and moderate heating leakage runs settle into a more compact stalled-shock state. As $f_{\rm heat}$ is increased, the leakage solutions display progressively stronger deviations from the more weakly heated cases. The models with $f_{\rm heat} = 1.55$ and 1.60 develop pronounced oscillatory behavior during the intermediate and late post-bounce phases. These oscillations likely reflect the dynamical response of the stalled shock to the competition between accretion ram pressure and neutrino-driven pressure support in the gain region. In physical terms, they can be interpreted as signatures of a marginal state in which the shock is neither steadily receding nor entering a clean runaway expansion, but instead undergoes repeated expansion–contraction cycles. Such behavior is expected when the post-shock flow becomes highly sensitive to modest changes in heating efficiency. For still larger heating factors the shock evolution changes qualitatively. The $f_{\rm heat} = 1.70$ model shows late-time outward growth after roughly 200 ms and reaches several hundred kilometers by the end of the simulation. The $f_{\rm heat} = 1.80$ model exhibits the strongest expansion, growing rapidly after $\sim$ 200 ms and reaching $\sim$ 1100–1200 km by 300 ms. These trajectories are characteristic of shock revival and runaway expansion. If the Two-Moment curve is taken as the approximated Boltzmann reference solution, then the figure suggests that the leakage prescription requires an effective enhancement of the heating strength in order to approach the more extended shock evolution obtained with the two-moment transport. At the same time, the comparison also shows a limitation of the leakage approach to match the overall shock radius history is not equivalent to reproducing the full temporal structure of the transport solution. In particular, the oscillatory behavior seen in the high-$f_{\rm heat}$ leakage runs appears stronger and more explicit than in the Two-Moment curve, indicating that the calibrated leakage model may capture the gross trend of shock support while still differing in the detailed time-dependent response of the post-shock flow.

3.3 Calibration of the Leakage Heating Factor

The heating-factor range was selected to bracket the transition from insufficient neutrino heating to excessively strong heating that leads to artificial shock revival in one-dimensional leakage simulations. In the leakage prescription, $f_{\rm heat} = 1$ corresponds to the nominal heating rate, while values greater (smaller) than unity enhance (reduce) the neutrino energy deposition [43]. Since the leakage models with heating factors close to unity already produce shock radii systematically smaller than those obtained with the two-moment reference calculation, values below unity were not expected to improve the agreement and were therefore not explored. As $f_{\rm heat}$ is increased, the leakage shock trajectory progressively approaches the two-moment result. Starting at approximately $f_{\rm heat} \simeq 1.4$, the shock remains at larger radii and begins to show a dynamical response closer to the reference evolution, while the agreement improves further in the range $f_{\rm heat} \simeq 1.5$–1.6. Therefore, the sampling was made finer in this interval in order to resolve the transition more accurately. Among the tested values, $f_{\rm heat} = 1.60$ provides the best overall agreement with the two-moment calculation, maintaining the shock radius near $\sim$ 200 km during approximately 250–300 ms post-bounce while avoiding the artificial runaway expansion that appears for $f_{\rm heat} \gtrsim 1.7$. This behavior, to-

gether with the statistical measures discussed below, motivates our adoption of $f_{\rm heat} = 1.60$ for the subsequent two-dimensional simulations. The neutrino heating efficiency adopted in leakage schemes is not derived from first principles, but instead acts as an effective parameter that compensates for the simplified treatment of neutrino transport. Consequently an appropriate calibration is required before employing the leakage approximation in multidimensional simulations. In this work, the calibration is performed by comparing the temporal evolution of the shock radius obtained with the leakage scheme against the reference solution produced by the `Flash-X` coupled with the `thornado` two-moment neutrino transport. For each heating factor, the leakage shock radius is interpolated onto the temporal grid of the corresponding two-moment simulation. Quantitative similarity between the two shock trajectories is then evaluated using several complementary statistical measures. The primary metric used in this work is the root-mean-square error (RMSE),

$$\mathrm{RMSE} = \sqrt{\frac{1}{N}\sum_{i=1}^{N}\left(R_{\mathrm{L},i} - R_{\mathrm{T},i}\right)^2}, \tag{31}$$

where $R_{\rm L}$ and $R_{\rm T}$ denote the shock radii obtained with the leakage and two-moment transport schemes, respectively, and N is the number of common temporal samples. The RMSE measures the overall deviation between the two shock trajectories over the complete post-bounce evolution. Since large deviations contribute quadratically, this metric is particularly sensitive to significant disagreements in shock evolution and therefore provides a robust measure of global agreement. To complement the RMSE, the mean absolute error (MAE) is also calculated,

$$\mathrm{MAE} = \frac{1}{N}\sum_{i=1}^{N}\left|R_{\mathrm{L},i} - R_{\mathrm{T},i}\right|. \tag{32}$$

Unlike the RMSE, the MAE assigns equal weight to all deviations and is therefore less influenced by isolated large discrepancies. Together, RMSE and MAE provide complementary measures of the average agreement between the two transport methods. The maximum absolute deviation is further evaluated as

$$\Delta R_{\max} = \max\left|R_{\rm L} - R_{\rm T}\right|, \tag{33}$$

which quantifies the largest instantaneous difference between the two shock trajectories. This metric is useful for identifying whether a particular heating factor produces localized deviations even when the average agreement remains acceptable. Because the shock radius evolves over several orders of magnitude during the post-bounce phase, a normalized error measure is also introduced. The relative RMSE is defined as

$$\text{Relative RMSE} = 100\sqrt{\frac{1}{N}\sum_{i=1}^{N}\left(\frac{R_{\mathrm{L},i} - R_{\mathrm{T},i}}{R_{\mathrm{T},i}}\right)^2}, \tag{34}$$

which expresses the overall discrepancy as a percentage of the reference shock radius. This normalization enables direct comparison between simulations exhibiting different characteristic shock sizes. For completeness, the Pearson correlation coefficient,

$$r = \frac{\sum\left(R_{\rm L} - \overline{R}_{\rm L}\right)\left(R_{\rm T} - \overline{R}_{\rm T}\right)}{\sigma_{\rm L}\sigma_{\rm T}}, \tag{35}$$

was also computed. In this expression, r is the Pearson correlation coefficient. Mean values are given by $\overline{R}_{\rm L}$ and $\overline{R}_{\rm T}$, and $\sigma_{\rm L}$ and $\sigma_{\rm T}$ are the corresponding standard deviations. A value

Table 3: Comparison of the shock-radius evolution obtained with the leakage scheme for different heating factors against the reference FLASH-X/`Thornado` simulation. The preferred heating factor is highlighted in bold.

Heating Factor	RMSE (10^6 cm)	MAE (10^6 cm)	Max Error (10^6 cm)	Relative RMSE (%)	Peak Difference (10^6 cm)	Correlation
1.05	9.26	8.62	14.56	46.87	−10.27	−0.159
1.10	9.08	8.39	14.49	45.92	−9.79	−0.159
1.30	8.16	7.17	14.24	41.14	−7.10	−0.115
1.40	7.45	6.21	14.10	37.58	−5.20	−0.050
1.50	6.30	5.05	13.95	31.82	−2.75	0.073
1.55	5.27	4.13	13.90	26.78	−1.46	0.189
1.60	**4.35**	**3.32**	**13.83**	**21.89**	**0.71**	**0.335**
1.70	8.81	7.41	16.99	44.59	12.77	0.399
1.80	15.23	12.08	45.35	77.58	40.61	0.369

of r close to unity indicates that both models exhibit a strongly similar temporal trend in shock evolution. Although this coefficient measures the similarity of the overall temporal trends, it is not adopted as the primary calibration criterion because small temporal shifts between similar shock trajectories can substantially reduce the correlation coefficient while having little physical significance. Consequently, correlation is used only as a qualitative indicator of the similarity between the two solutions. Finally the maximum shock radius reached during the post-bounce evolution is compared between the leakage and two-moment approximation simulations,

$$\Delta R_{\rm peak} = R^{\rm L}_{\rm peak} - R^{\rm T}_{\rm peak}. \tag{36}$$

The peak shock radius provides a physically intuitive measure of the overall explosion strength predicted by each heating factor and serves as an additional validation of the leakage calibration. Among all investigated heating factors, the preferred value is selected according to the smallest RMSE together with the smallest relative RMSE, while simultaneously reproducing the peak shock radius of the reference two-moment approximation simulation. This multi-criterion approach ensures that the selected heating factor reproduces not only the average shock evolution but also the overall dynamical behavior of the post-bounce shock. The calibrated heating factor is subsequently adopted in the two-dimensional leakage simulations presented in this work (see Section 3.4). As summarized in Table 3, the leakage solution approaches the reference two-moment approximation model as the heating factor increases from 1.05 to 1.60. Both the RMSE and MAE decrease monotonically over this interval, indicating an increasingly accurate reproduction of the shock-radius evolution. The relative RMSE is reduced from approximately 47% for a heating factor of 1.05 to only 22% for a heating factor of 1.60, while the difference in the peak shock radius decreases from more than 10^7, cm to only 7.1×10^5, cm. Further increasing the heating factor beyond 1.60 leads to a rapid deterioration of the agreement with the reference solution. In particular, the RMSE nearly doubles for a heating factor of 1.70 and exceeds 1.5×10^7, cm for a heating factor of 1.80. This behavior reflects an excessive neutrino heating rate, causing the shock to expand significantly beyond the evolution predicted by the two-moment transport calculation. Although the Pearson correlation coefficient continues to increase slightly for heating factors larger than 1.60, this quantity is not used as the primary calibration criterion because it measures similarity in the overall temporal trend rather than the absolute agreement of the shock radius. For the purpose of reproducing the reference two-moment approximation solution, the RMSE, relative RMSE, and peak shock radius provide more

physically meaningful measures of agreement. Based on these criteria, a heating factor of $f_{\rm heat} = 1.60$ provides the best overall match and is therefore adopted in all subsequent two-dimensional leakage simulations.

3.4 Two Dimensional Simulation of $15M_\odot$ with the Heating Factor of 1.6 by the Leakage Scheme

Figure 7 shows the temporal evolution of the entropy distribution in the meridional plane for the 2D model evolved with the calibrated heating factor $f_{\rm heat} = 1.6$. The six panels correspond to post-bounce times of $t_{\rm pb} = 0$, 38, 76, 114, 152, and 190 ms, and illustrate the gradual transition from a nearly spherical post-bounce configuration to a strongly aspherical, multi-dimensional flow. At $t_{\rm pb} = 0$ ms, the entropy field is still relatively smooth and centrally concentrated reflecting the early post-bounce structure. As time advances, the shock expands outward and the region behind it becomes increasingly structured with high-entropy material filling the gain region and low-entropy accretion streams penetrating inward from larger radii. By $t_{\rm pb} \approx 38 - 76$ ms the shock has clearly moved beyond the inner

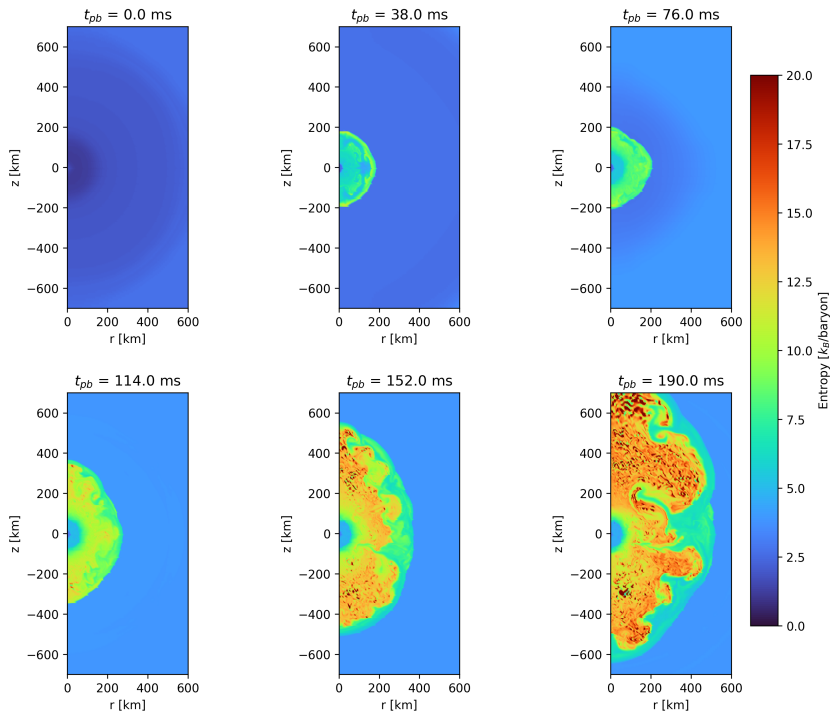

Figure 7: Temporal evolution of the specific entropy in the 2D post-bounce simulation of the $15\,M_\odot$ progenitor with the calibrated heating factor $f_{\rm heat} = 1.6$. The panels show snapshots at $t_{\rm pb} = 0$, 38, 76, 114, 152, and 190 ms. The color map represents the entropy in units of $k_{\rm B}$ per baryon. The sequence illustrates the outward expansion of the shock, the growth of high-entropy plumes in the gain region, and the transition to a strongly asymmetric post-shock flow. By $t_{\rm pb} = 190$ ms, the shock has expanded beyond ~ 500 km.

~ 200 km and the post-shock layer begins to develop pronounced angular variations. This marks the onset of vigorous multi-dimensional activity, where neutrino heating and advection

interact to produce buoyant high-entropy plumes. At $t_{\rm pb} = 114$ ms these plumes become more prominent and extend to larger radii, indicating that heated matter is rising efficiently through the gain region and pushing the shock outward. The flow is no longer close to spherical symmetry and the entropy map reveals the onset of large-scale asymmetries that are characteristic of neutrino-driven convection and shock deformation. At the later times $t_{\rm pb} = 152$ and 190 ms the shock front has expanded to radii of several hundred kilometers (~ 500 km) and the post-shock region is dominated by strong entropy contrasts. The largest high-entropy structures occupy much of the polar extent of the computational domain, while cooler downflows continue to feed the proto-neutron-star vicinity simultaneously which was not viable in 1D. In the final panel, the shock has moved beyond ~ 500 km demonstrating that the calibrated heating prescription with $f_{\rm heat} = 1.6$ is sufficient to drive sustained shock expansion in the 2D model. This sequence highlights how the same heating strength that was calibrated against the 1D Two-Moment reference leads, in two dimensions, to the development of buoyancy-driven plumes and enhanced entropy production with the strongly non-spherical post-shock flow.

Figure 8 compares the post-bounce evolution of the mean shock radius in the one-dimensional `Flash-X` coupled with `thornado` (two-moment approximation) model and the two-dimensional `FLASH 4.6.2` with the leakage calculation. The two simulations exhibit very similar early-time behavior and in both cases the shock initially expands to $\sim$ 230–250 km within the first $\sim$ 10–20 ms after bounce, followed by a temporary contraction to $\sim$ 160–180 km over the next few tens of milliseconds. This early agreement indicates that the calibrated heating prescription reproduces the gross post-bounce shock evolution reasonably well in the spherically symmetric limit. At later times the two models diverge by

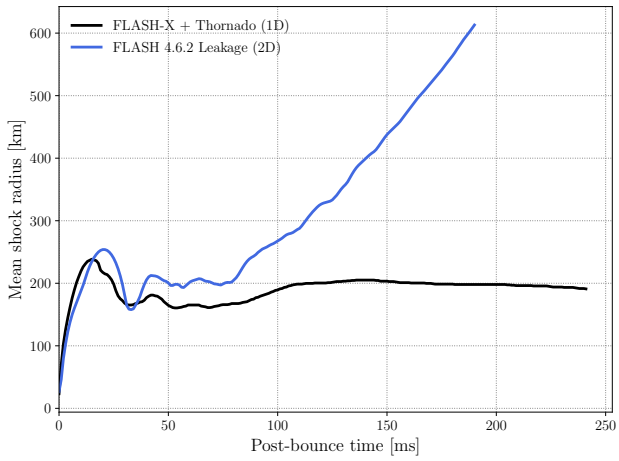

Figure 8: Comparison of the mean shock radius as a function of post-bounce time for the 1D `Flash-X` coupled with `thornado` model (black) and the 2D `FLASH 4.6.2` with the leakage model (blue). Both simulations show an initial shock expansion followed by a brief recession, but their late-time evolution differs strongly. The 1D shock stalls near $\sim$ 200 km, whereas the 2D model undergoes sustained expansion and reaches $\sim$ 600 km by $\sim$ 200 ms, indicating successful shock revival in two dimensions.

far in the mean shock radius. In the 1D two-moment the mean shock radius remains nearly stationary at $\sim$ 190–205 km for the remainder of the plotted interval, consistent with a stalled shock and the absence of a successful explosion in spherical symmetry. By contrast

the 2D leakage model undergoes sustained shock re-expansion after $\sim$ 80–100 ms and enters a runaway growth phase, reaching several hundred kilometers by $\sim$ 150 ms and $\sim$ 600 km by $\sim$ 200 ms. This separation demonstrates the crucial role of multidimensional effects in reviving the shock, non-radial hydrodynamic instabilities and the resulting increase in dwell time within the heating region allow the same overall heating strength to drive explosion in two dimensions, while the corresponding 1D model remains marginal and ultimately stalled.

3.4.1 Explosion mechanism: neutrino heating, convection, and SASI

The revival of the stalled shock in core-collapse supernovae is governed by the competition between neutrino heating, accretion ram pressure, and multi-dimensional hydrodynamic instabilities. In the neutrino-heating mechanism the electron-flavor neutrinos emitted from the proto-neutron star deposit energy in the gain region through charged-current absorption reactions:

$$\nu_e + n \rightarrow p + e^-,$$

$$\bar{\nu}_e + p \rightarrow n + e^+.$$

The deposited neutrino energy increases the entropy of the matter behind the shock and produces buoyant high entropy bubbles. These rising structures modify the accretion flow, reduce the effective radial velocity, and increase the residence time of matter in the gain region. Consequently, a larger amount of material can absorb neutrino energy and eventually leading to runaway shock expansion. To analyze the explosion mechanism of the two-dimensional leakage simulation we using the shock evolution with neutrino heating timescale, advection timescale, and hydrodynamic mode amplitudes. The combined diagnostics indicate that the explosion is driven by neutrino-heating assisted convection rather than by a direct neutrino momentum deposition or a SASI-dominated instability. For the heating timescale we use [7]:

$$\tau_{\rm heat} = \frac{|\epsilon_{\rm g}|}{Q_\nu^+}, \tag{37}$$

where $\epsilon_{\rm g}$ and Q_ν^+ are the gravitational binding energy and heating rate respectively which $Q_\nu^+ \propto \sum_i L_{\nu_i} \left\langle \epsilon_{\nu_i}^2 \right\rangle r^{-2}$ is the summation over all neutrino types luminosities and average energy. For the advection timescale one can write:

$$\tau_{\rm adv} = \frac{M_{\rm gain}}{\dot{M}}, \tag{38}$$

where $M_{\rm gain}$ refers to the mass in the gain region which is between the neutrino sphere ($R_{\rm ns} = R_{(\tau_{\nu_i}=2/3)}$) and shock radius. $\dot{M}$ is the mass accretion rate. The Figure 9 shows the evolution of the ratio of $\tau_{\rm adv}/\tau_{\rm heat}$ which is increasing until 180 ms post-bounce that exceeds the unity which is favorable to the explosion which means the dwell time for the mass in the gain region to absorb energy by neutrinos from the proto-neutron star is enough. Now with favorable timescale we need to check the criteria for the convection in the gain region behind the shock. The growth of the convective instability is quantified using the Foglizzo [44] parameter,

$$\chi = \int_{R_{\rm gain}}^{R_{\rm shock}} \frac{\omega_{\rm BV}}{|v_r|} dr, \tag{39}$$

where $\omega_{\rm BV}$ is the Brunt–Väisälä frequency. For

$$\chi > 3, \tag{40}$$

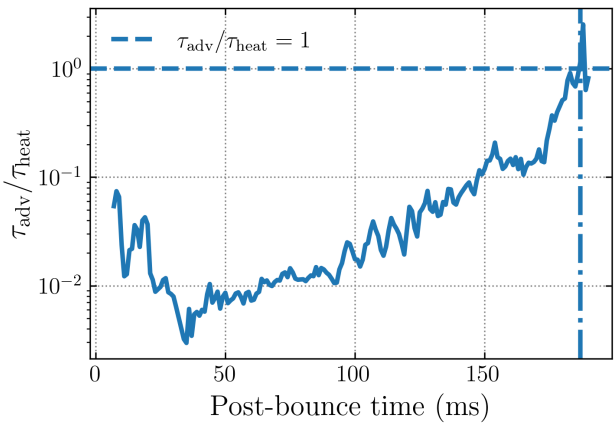

Figure 9: The time evolution of $\tau_{\rm adv}/\tau_{\rm heat}$ of the $15M_\odot$ progenitor in 2D that is increasing and exceeds the threshold of unity at time of 180 ms.

convective perturbations can grow before matter leaves the gain region. In our simulation, χ exceeds this critical value, indicating that convection is well developed before shock runaway. It is shown in the Figure 10 (upper-right) $\chi > 3$ is fulfilled around 150 ms.

To investigate the contribution of the standing accretion shock instability (SASI), we analyze the spherical harmonic mode amplitudes of the shock front $R_s(\theta, t)$. One can write the Legendre decomposition as follows:

$$a_l(t) = \frac{2l+1}{2} \int R_s(\theta, t) P_l(\cos\theta) d\cos\theta \tag{41}$$

and we consider the first two important order ratio of a_1/a_0 for the $= 1, 2$ which corresponds to the sloshing and the deformation of the shock [45]. As we can Figure 10 (lower-right) for both $= 1$ and $= 2$ we see no growth in the amplitude ratio of a_1/a_0. So SASI is not the reason for the explosion here in this study of $15M_\odot$ progenitor.

The overall explosion sequence can therefore be summarized as neutrino heating in the gain region increases the entropy of the post-shock material, thereby generating buoyant motions ($\omega_{\rm BV} < 0$). The resulting buoyancy drives neutrino-driven convection and produces rising, high-entropy plumes. These nonradial motions hinder the direct advection of matter through the gain region toward the proto-neutron star and consequently increase the advection timescale, $\tau_{\rm adv}$. The longer residence time allows the accreted material to absorb more energy from the neutrino radiation field. When the advection timescale becomes longer than the characteristic heating timescale, such that

$$\frac{\tau_{\rm adv}}{\tau_{\rm heat}} > 1,$$

matter remains in the gain region long enough (see lower-left of Figure 10 for the growth of hte mass in the gain region) to acquire sufficient energy to overcome its gravitational binding. The enhanced thermal pressure behind the shock then promotes sustained shock expansion, eventually leading to shock runaway and the onset of a successful neutrino-driven explosion. Thus, our two-dimensional leakage simulation supports a neutrino-heating-assisted convective explosion mechanism, where neutrino heating provides the energy source while convection enhances the efficiency of energy deposition and facilitates shock revival.

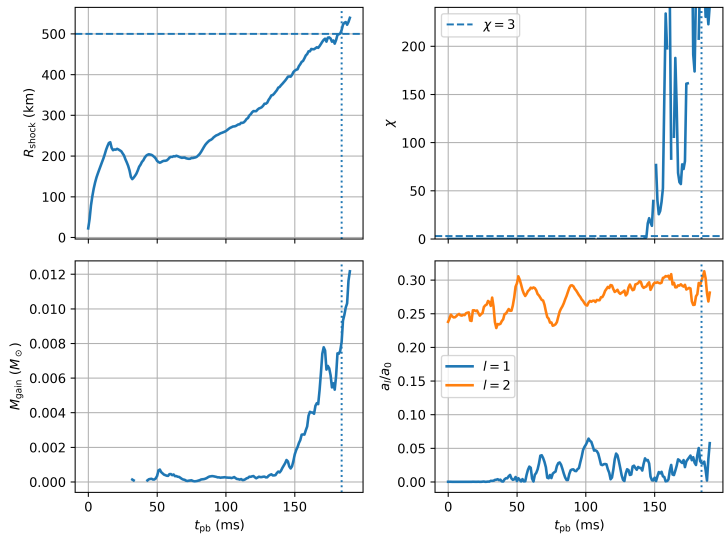

Figure 10: Core-collapse supernova diagnostics as functions of post-bounce time, $t_{\rm pb}$. From top left to bottom right, the panels show the shock radius $R_{\rm shock}$, the diagnostic parameter χ, the gain-region mass $M_{\rm gain}$, and the normalized amplitudes of the $l = 1$ and $l = 2$ modes, a_l/a_0. The horizontal dashed line in the upper-left panel marks $R_{\rm shock} = 500$ km, while the dashed reference in the upper-right panel indicates $\chi = 3$. The vertical dotted line in all panels marks a reference time of $t_{\rm pb} \approx 185$ ms.

Although neutrino heating provides the energy source, multi-dimensional convection plays a crucial role in enhancing the heating efficiency. The entropy and radial velocity structures (Fig. 11) show buoyant high-entropy regions and rising plumes behind the shock. These structures are signatures of neutrino-driven convection as the velocity stream lines are showing.

4 Discussion and Conclusions

In this study we simulate the collapse and post-bounce evolution of a 15 $M_\odot$ progenitor using two numerical approaches. A spherically symmetric reference simulation was performed by `Flash-X` coupled to `thornado`, using energy-dependent two-moment neutrino transport, while a computationally less expensive multispecies neutrino-leakage scheme implemented in `FLASH 4.6.2` was used for both one- and two-dimensional calculations. The leakage method includes approximate neutrino emission, cooling, deleptonization, and absorption heating with the strength of the latter controlled by the parameter $f_{\rm heat}$. We calibrated this parameter by comparing the time-dependent shock radius in a series of 1D leakage calculations with the corresponding `Flash-X/thornado` result. The calibrated value, $f_{\rm heat} = 1.60$, was then used without further adjustment in the 2D simulation.

The `Flash-X/thornado` calculation reproduces the principal features expected during stellar-core collapse and the early post-bounce phase. The central density rises from approximately $10^{10}\,{\rm g\,cm^{-3}}$ to nuclear density, at which point the stiffening of the equation of state halts the homologously collapsing inner core and launches a hydrodynamic shock. The radial profiles show the associated velocity discontinuity and entropy production, as

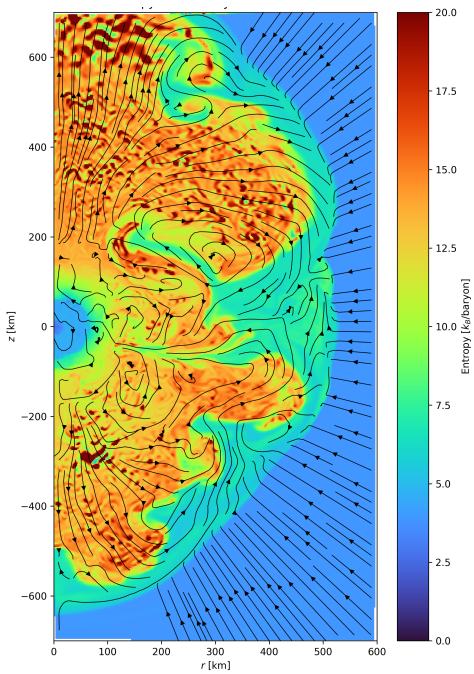

Figure 11: Entropy distribution in the r-z plane, shown with a color map of the specific entropy and overlaid velocity streamlines. The streamlines reveal the development of buoyant plumes and convective motions behind the shock, rather than a simple uniform outward radial flow at the shock surface. In this multidimensional flow pattern, shock expansion is driven primarily by convection and plume dynamics, which help sustain shock growth during the post-bounce phase.

well as the strong deleptonization caused by electron capture and neutrino emission. After formation, the shock initially expands but loses energy through nuclear dissociation, and continued interaction with the accretion flow. It consequently settles into a stalled configuration at a characteristic radius of approximately 190–200 km. The simultaneous evolution of the density, velocity, entropy, electron fraction, mass-accretion rate, and neutrino luminosity provides a mutually consistent description of the formation of the proto-neutron star and the development of the post-bounce accretion flow.

The heating-factor survey demonstrates that the shock evolution predicted by the leakage approximation is sensitive to the effective neutrino-heating strength. For $f_{\rm heat} \lesssim 1.5$, the initial shock expansion is followed by substantial recession, and the leakage models produce shock radii systematically smaller than those of the two-moment calculation. Increasing $f_{\rm heat}$ improves the agreement up to $f_{\rm heat} = 1.60$, for which the RMSE, MAE, and relative RMSE reach their minimum values among the tested models, while the peak shock radius is also reproduced to within 7.1×10^5 cm. Larger heating factors lead to excessive shock support and the models with $f_{\rm heat} = 1.70$ and 1.80 depart from the reference solution and eventually undergo strong shock expansion. The nonmonotonic dependence of the errors on $f_{\rm heat}$ therefore provides a well-defined calibration region rather than merely placing a lower limit on the required heating efficiency.

A result of this study is the qualitative difference of the explodability between the 1D and 2D obtained with comparable effective heating. In spherical symmetry the shock re-

mains stalled near 200 km while for the 2D leakage model with $f_{\rm heat} = 1.60$ it develops sustained shock expansion and reaches approximately 500–600 km by $t_{\rm pb} \simeq 190$–200 ms.It demonstrates how multidimensional hydrodynamics can modify the efficiency with which neutrino-deposited energy supports the shock.

The entropy color map and velocity streamlines shows the physical origin of this behavior. Neutrino absorption raises the entropy of matter in the gain region and establishing buoyant high-entropy structures behind the shock. These structures rise and merge into large plumes, while cooler and lower-entropy material continues to accrete through narrower downflows simultaneously which was not possible in 1D model. The resulting flow is strongly nonradial and does not resemble a uniform outward acceleration of matter at the shock surface. Thus neutrino heating acts primarily as the energy source that establishes an unstable entropy stratification, while buoyancy and convection redistribute the heated material and generate the pressure support required for shock expansion. The morphology consequently argues against interpreting shock revival as the result of direct neutrino momentum deposition or an instantaneous outward radial velocity imposed at the shock.

The timescale and instability diagnostics support this interpretation. The Foglizzo parameter becomes larger than the approximate critical value $\chi \simeq 3$, indicating that buoyant perturbations have sufficient time to grow while being advected through the gain region. At the same time, the gain mass increases as the expanding shock enlarges the volume available for neutrino heating. Convective circulation and rising plumes reduce the effective radial advection speed and increase the residence time of material behind the shock. The resulting growth of $\tau_{\rm adv}$ eventually causes $\tau_{\rm adv}/\tau_{\rm heat}$ to exceed unity near $t_{\rm pb} \simeq 180$–185 ms. Under these conditions, matter remains in the gain region long enough to absorb an amount of neutrino energy comparable to or larger than its binding energy, favoring runaway shock expansion.

The low-order deformation amplitudes have no evidence that the explosion is dominated by the standing accretion shock instability. Neither the $l = 1$ nor the $l = 2$ normalized mode exhibits the sustained, coherent growth expected for a strongly SASI-dominated flow before shock runaway. The combined evidence from the entropy morphology, velocity streamlines, Foglizzo parameter, gain-region mass, heating-to-advection timescale ratio, and low-order shock modes instead favors a neutrino-heating assisted convective mechanism. Nevertheless, convection and SASI are not strictly independent phenomena, and short-lived oscillations or nonlinear coupling between the two cannot be excluded solely from the first two mode amplitudes. Our conclusion is therefore that SASI is not the dominant driver in this simulation, rather than that it is entirely absent.

Several important results can be listed as follows. First, the leakage heating factor is constrained through a quantitative comparison with an energy-dependent two-moment calculation instead of being selected only to obtain an explosion. Second, the use of multiple error metrics reduces the risk that the calibration is controlled by a single feature of the shock trajectory. Third, the transition from a stalled 1D shock to an expanding 2D shock is assessed using several independent hydrodynamic and thermodynamic diagnostics. Finally, the leakage approach makes it possible to investigate multidimensional instability growth at substantially lower computational cost than a comparable multidimensional spectral-transport calculation.

The results must, however, be interpreted in light of several limitations. The leakage scheme does not evolve the full angular and spectral neutrino distribution and approximates the transition between optically thick and free-streaming regimes. The factor $f_{\rm heat}$ absorbs inaccuracies arising from these approximations and should not be regarded as a universal physical constant. Its calibrated value can depend on the progenitor, equation of state, numerical resolution, weak-interaction rates, gravity treatment, and the reference transport

implementation. Moreover, calibrating only the shock radius does not guarantee simultaneous agreement in the neutrino luminosities, mean neutrino energies, electron-fraction distribution, gain radius, heating efficiency, or proto-neutron-star contraction. The remaining relative RMSE of approximately 22% also shows that the calibrated leakage model reproduces the global reference evolution only approximately.

Additional limitations arise from dimensionality and simulation duration. In axisymmetry, turbulent energy can accumulate artificially in large-scale structures because of the inverse turbulent cascade, potentially producing more coherent plumes and facilitating shock expansion relative to 3D. The explosion time and shock-growth rate obtained here may therefore not carry over quantitatively to three dimensions.

Future work should extend the calibration to a broader set of progenitors and compare not only the shock radius but also neutrino luminosities and spectra, gain-region heating, proto-neutron-star contraction, and electron-fraction evolution.

4.1 Limitations of the Comparison

The comparisons presented in this work should be interpreted with several important limitations in mind. First, the reference and leakage calculations are not performed within an identical numerical framework. The reference one-dimensional model employs `Flash-X` coupled to the `thornado` spectral two-moment neutrino-transport solver, whereas the leakage calculations are carried out with `FLASH 4.6.2` using an approximate neutrino leakage and heating prescription. Consequently, differences between the corresponding shock trajectories cannot be attributed exclusively to the neutrino-transport method. Differences in the hydrodynamic solver, spatial discretization, adaptive-mesh treatment, gravity implementation, and other numerical details may also contribute to the quantitative differences between the simulations. For this reason, the present calibration should be regarded as an effective cross-code calibration of the shock evolution rather than a strict one-to-one comparison in which only the neutrino-transport prescription is varied.

A second limitation arises from the fundamentally different treatment of neutrino radiation. The two-moment calculation evolves an energy-dependent neutrino radiation field, whereas the leakage scheme estimates neutrino emission, diffusion, and absorption using local and energy-integrated prescriptions. Therefore, agreement in the shock radius does not necessarily imply comparable neutrino luminosities, mean neutrino energies, electron-fraction profiles, gain radii, heating efficiencies, or proto-neutron-star contraction. The calibrated value of f_{heat} should consequently not be interpreted as a universal physical constant, since its preferred value may depend on the progenitor, equation of state, spatial resolution, gravity treatment, weak-interaction rates, and the particular reference transport implementation.

Finally, the calibration is obtained from one-dimensional simulations and is subsequently applied without further adjustment to the two-dimensional leakage calculation. This procedure allows us to investigate the role of multidimensional hydrodynamics at substantially reduced computational cost, but it does not constitute a direct comparison between one- and two-dimensional simulations employing the same neutrino-transport method. Non-radial effects such as neutrino-driven convection, turbulent motions, and shock deformation are absent by construction in spherical symmetry and become dynamically important in two dimensions. In addition, axisymmetric turbulence can favor the development of large-scale structures through the inverse turbulent cascade, so the explosion time and shock-expansion rate obtained in 2D should not be assumed to carry over quantitatively to fully three-dimensional calculations. A fully controlled assessment would require simulations with the same hydrodynamic framework, microphysics, resolution, and neutrino-transport treatment

in both one and multiple spatial dimensions.

Acknowledgment

We gratefully acknowledge Ferdowsi Cloud (`https://ferdowsi.cloud/en`) for providing cloud computing resources, and the High Performance Computing Center of the University of Mazandaran (`https://it.umz.ac.ir/hpc`) for access to high-performance computing facilities that enabled the simulations in this work.

Authors' Contributions

All authors have contributed equally to the conceptualization, methodology, software development, and writing of this manuscript.

Data Availability

No data available.

Conflicts of Interest

The authors declare that there is no conflict of interest.

Ethical Considerations

The authors have diligently addressed ethical concerns, such as informed consent, plagiarism, data fabrication, misconduct, falsification, double publication, redundancy, submission, and other related matters.

Funding

This research did not receive any grant from funding agencies in the public, commercial, or non profit sectors.

References

[1] Woosley, S., & Janka, T. 2005, Nature Physics, 1, 147.

[2] O'Connor, E., & Ott, C. D. 2011, ApJ, 730, 70.

[3] Nomoto, K., Kobayashi, C., & Tominaga, N. 2013, ARA&A, 51, 457.

[4] Baade, W., & Zwicky, F. 1934, Proceedings of the National Academy of Science, 20, 259.

[5] Bethe, H. A. 1990, Reviews of Modern Physics, 62, 801.

[6] Arnett, W. D. 1996, Supernovae and Nucleosynthesis, Princeton University Press.

[7] Janka, H.-T. 2012, Annual Review of Nuclear and Particle Science, 62, 407.

[8] Colgate, S. A., & White, R. H. 1966, ApJ, 143, 626.

[9] Burrows, A., et al. 2007, ApJ, 664, 416.

[10] Müller, B. 2016, PASA, 33, e048.

[11] Nordhaus, J., Burrows, A., Almgren, A., & Bell, J. 2010, The Astrophysical Journal, 720, 694.

[12] Rampp, M., & Janka, H.-T. 2002, A&A, 396, 361.

[13] Just, O., Obergaulinger, M., & Janka, H.-T. 2015, Monthly Notices of the Royal Astronomical Society, 453, 3387.

[14] Ruffert, M., Janka, H.-T., Takahashi, K., & Schaefer, G. 1997, A&A, 319, 122.

[15] Rosswog, S., Ramirez-Ruiz, E., & Davies, M. B. 2003, Monthly Notices of the Royal Astronomical Society, 345, 1077.

[16] O'Connor, E., & Ott, C. D. 2011, The Astrophysical Journal, 730, 70.

[17] Couch, S. M., & O'Connor, E. P. 2014, The Astrophysical Journal, 785, 123.

[18] Fryxell, B., et al. 2000, The Astrophysical Journal Supplement Series, 131, 273.

[19] Couch, S. M. 2013, The Astrophysical Journal, 775, 35.

[20] Lee, D., Deane, A. E., & Federrath, C. 2009, Numerical Modeling of Space Plasma Flows: ASTRONUM-2008, Vol. 406 of Astronomical Society of the Pacific Conference Series, edited by Pogorelov, N. V., Audit, E., Colella, P., & Zank, G. P. PUBLISHER, p. 243.

[21] Lee, D. 2013, Journal of Computational Physics, 243, 269.

[22] Colella, P., & Woodward, P. R. 1984, Journal of Computational Physics, 54, 174.

[23] Liebendörfer, M. 2005, The Astrophysical Journal, 633, 1042.

[24] O'Connor, E., & Ott, C. D. 2010, Classical and Quantum Gravity, 27, 114103.

[25] Janka, H.-T. 2001, A&A, 368, 527.

[26] MacNeice, P., et al. PARAMESH: A parallel adaptive mesh refinement community toolkit, 2000, version 1, Mendeley Data.

[27] Dubey, A., et al. 2022, SoftwareX, 19, 101168.

[28] Endeve, E., et al. 2019, Journal of Physics: Conference Series, 1225, 012014.

[29] Harris, J. A., et al. 2022, The International Journal of High Performance Computing Applications, 36, 59.

[30] LeVeque, R. J. 2002, Finite Volume Methods for Hyperbolic Problems, Cambridge Texts in Applied Mathematics, Cambridge University Press.

[31] Laiu, M. P., et al. 2021, The Astrophysical Journal Supplement Series, 253, 52.

[32] Chu, R., Endeve, E., Hauck, C. D., & Mezzacappa, A. 2019, Journal of Computational Physics, 389, 62.

[33] Chu, R., et al. 2019, Journal of Physics: Conference Series, 1225, 012013.

[34] Paul Laiu, M., Harris, J. A., Chu, R., & Endeve, E. 2020, Journal of Physics: Conference Series, 1623, 012013.

[35] Pareschi, L., & Russo, G. Implicit-explicit Runge-Kutta schemes and applications to hyperbolic systems with relaxation, 2010.

[36] Couch, S. M., et al. 2021, Parallel Computing, 108, 102830.

[37] Balsara, D. S., Garain, S., & Shu, C.-W. 2016, Journal of Computational Physics, 326, 780.

[38] MacNeice, P., et al. PARAMESH V4.1: Parallel Adaptive Mesh Refinement, Astrophysics Source Code Library, record ascl:1106.009, 2011.

[39] Steiner, A. W., Lattimer, J. M., & Brown, E. F. 2010, The Astrophysical Journal, 722, 33.

[40] Steiner, A. W., Hempel, M., & Fischer, T. 2013, The Astrophysical Journal, 774, 17.

[41] Bruenn, S. W. 1985, ApJS, 58, 771.

[42] Woosley, S. E., & Heger, A. 2015, ApJ, 810, 34.

[43] Couch, S. M., & O'Connor, E. P. 2014, The Astrophysical Journal, 785, 123.

[44] Foglizzo, T., Scheck, L., & Janka, H.-T. 2006, The Astrophysical Journal, 652, 1436.

[45] Burrows, A., Dolence, J. C., & Murphy, J. W. 2012, The Astrophysical Journal, 759, 5.